Retrieval of Parameters for Layered non-Smooth Interface Media: Theory and Experiment

by

Yuriy M Goykhman

A dissertation submitted in partial fulfillment
of the requirements for the degree of
Doctor of Philosophy
(Electrical Engineering)
in The University of Michigan
2011

Doctoral Committee:

Professor Mahta Moghaddam, Chair
Professor Anthony Grbic
Professor Valeriy Ivanov
Professor Fawwaz T. Ulaby

To my family

ACKNOWLEDGEMENTS

I would like to thank my faculty advisor and committee chair, Professor Mahta Moghaddam for her wisdom and guidance during my graduate school years. I would also like to thank my committee: Professor Grbic, Professor Ivanov and Professor Ulaby for their invaluable advice, and for evaluating this work.

I would like to thank my wonderful colleagues at the Radiation Laboratory for their guidance, collaboration and friendship. Leland Pierce and Adib Nashashibi were always generous with their time, and never failed to supply useful insights. I would like to especially thank my colleague Xueyang Duan with whom I spent many hours designing, building, debugging the radar.

I would like to express my deepest gratitude to my wife Marina for her patience and support. I would also like to thank my parents, my brother and grandparents for their care and support.

TABLE OF CONTENTS

LIST OF FIGURES

Figure

LIST OF TABLES

Table

ABSTRACT

Retrieval of Parameters for Layered non-Smooth Interface Media: Theory and Experiment

by

Yuriy M Goykhman

Chair: Mahta Moghaddam

Many naturally occurring or manmade objects can be modeled as three layer media with non-smooth interfaces. Most of the existing forward and inverse scattering models that can be applied to such media are either too inefficient or have limited regions of validity. In this dissertation an efficient forward scattering model based on the Extended Boundary Condition Method (EBCM) is developed for a three layer medium. The boundary between the first and the second layers is periodic while the boundary between the second and third layers is rough. The model is then extended by including an arbitrarily shaped cylinder placed into the third layer. Both TM and TE polarizations and PEC and Dielectric cylinder cases are considered. The Method of Moments (MOM) is used to obtain an impedance matrix, which is then transformed into a T-matrix. The T-matrix is transformed into a scattering matrix and cascaded with scattering matrices for the periodic and rough interfaces to obtain a generalized scattering matrix for the total system. A solution to the inverse problem for a three-layer medium is developed using simulated radar data. The retrieval of the layered- medium parameters is accomplished by sequential nonlinear optimiza-

tion starting from the top layer and progressively characterizing the layers below. The optimization process is achieved by an efficient iterative technique built around the solution of the forward scattering problem. To be efficiently utilized in the inverse problem, the forward scattering model is simulated over a wide range of unknowns to obtain a complete set of subspace-based equivalent closed-form models that relate radar backscattering coefficients to the sought-for parameters, including the dielectric constants of each layer and the thickness of the middle layer. The inversion algorithm is implemented as a modified conjugate-gradient-based nonlinear optimization. It is shown that this technique results in accurate retrieval of surface and subsurface parameters, even in the presence of noise. To validate forward and inverse scattering models, a compact tower-based radar system is built. The data collected with the instrument is used to demonstrate sensitivity of radar measurements to changes in soil moisture and the potential for estimating surface and subsurface parameters.

CHAPTER I

Introduction

1.1 Motivation and Dissertation Objectives

There is a great need for practical and efficient systems that can remotely estimate root zone soil moisture and snow depth, detect buried or sunken objects, estimate the depth of fresh bodies of water, and be used in medical and industrial testing and imaging. Both national governments and private companies have devoted considerable resources to research in the area of microwave remote sensing. In particular, in 2014 NASA is planning to launch The Soil Moisture Active-Passive (SMAP) mission to map soil moisture on a global scale using combined radar and radiometer observations. The purpose of the system, which will operate at L-band, is to estimate surface soil moisture. The penetrating abilities of low frequency radiation make it an excellent candidate for subsurface measurements. To penetrate dense vegetation and estimate root-zone soil moisture down to approximately 1.2 meters, NASA is planning to launch a UHF synthetic aperture system as part of the Airborne Microwave Observatory of Subcanopy and Subsurface (AirMOSS) program.

Microwave radar instruement cannot measure the quantities of interest directly; it measures quantities proportional to the radar cross section of the scene from which the sought-for parameters must be extracted. Inverse scattering models are algorithms that allow for retrieval of the desired parameters from the measured quantities. These

algorithms typically involve multiple evaluations of forward scattering models, which relate the sought-for parameters as well as various ancillary parameters to the measured quantities. The goal of this dissertation is to develop a complete subsurface sensing system that encompasses efficient forward and inverse scattering models, and can be used to interpret data measured by the compact tower-based instrument.

1.2 Previous Work

There have been considerable efforts to develop accurate, versatile and computationally efficient forward and inverse scattering models that can be applied to practical remote sensing systems. Forward scattering models can usually be classified as analytical, numerical, or a hybrid of analytical and numerical approaches. One of the most popular analytical methods is the Small Perturbation Method (SPM) developed for a single rough interface by Rice in the early 1950s [1]. In recent years the method was extended to include higher order expansions [2] and applied to media with two or more rough interfaces [3]. Since SPM is a purely analytical model, it is computationally very efficient. However, since it is based on truncation of a series expansion, the range of validity of the model is limited to surfaces with small and slowly varying roughness. Fully numerical techniques, such as the Method of Moments (MOM), can in principle be applied to almost any distribution and roughness scale. When applied to rough surfaces, many realizations of the random rough surface are needed to fully capture surface statistics, resulting in added computational times. Moreover, when applied to finite surfaces, the accuracy of solution deteriorates due to edge diffraction (see [4]). The problem is exacerbated when this method is applied to more than one interface. The edge diffraction effects can be only partially remedied by using tapered incident field as was demonstrated in [5]. In addition, the surface needs to be densely discretized to ensure accuracy of solutions. Therefore, such methods are computationally expensive and are rarely used in inversion algorithms where multiple

evaluations of the forward problem are needed.

Methods such as the ones based on the Extended Boundary Condition Method are significantly more efficient than fully numerical methods, they account for high order scattering, and have a significantly greater region of validity [6] than the approximate analytical solutions. However, these methods are still significantly slower than analytical methods and are too computationally expensive to be of practical use in inversion algorithms.

When modeling scattering from objects, such as a collection of cylinders, the T-matrix technique first developled by Waterman [7] in the early 1960s for a single scatterer can be especially useful. T-matrix is convenient since it does not depend on the incidence angle or the location of the object, thereby reducing its dependence to only the properties of an object and the polarization of the incoming radiation. In many multiple scattering problems such as detection of objects behind an obstacle, through-the-wall imaging, tunnel detection, and ground penetrating radar applications, real world objects are often approximated as circular cylinders ([8], [9], [10]). The analytical expressions for a T-matrix of a circular cylinder are simple and widely reported but cannot adequately describe a scatterer with noncircular cross section, so a more versatile T-matrix method is needed. In [11] a similar approach to the one presented in this dissertation is used to obtain a T-matrix for the simplest case of a PEC cylinder for TM polarization.

Inversion algorithms can be generally classified as local or global optimization methods. Local optimization methods such as variations on Newton's method [12] and the Conjugate Gradient methods [13] are iterative methods which generally rely on gradients and partial derivatives to obtain the next estimate. Since numerical evaluation of derivatives is not accurate and accumulates error, these methods are best suited for situations where derivatives can be computed analytically. Local optimization methods usually converge rapidly (at least as compared to global methods)

but may get trapped in a local minimum and fail to converge to the correct solution. Global optimization methods, such as the Simulated Annealing method [14], are guaranteed to converge but may take hundreds of thousands of iteration to do so. With the tremendous increase in computational power in recent years, a number of new works have successfully applied global optimization algorithms to solve inverse scattering problems [14], [15]. While it is feasible to use global optimization methods, local optimization techniques are still preferred from the point of view of computational efficiency. The algorithm used in this dissertation is a local optimization algorithm that is based on a Conjugate Gradient method.

There has been a number of previous efforts to experimentally validate forward and inverse scattering models as well as to construct practical instruments to estimate soil moisture, detect burried objects and perform through-the-wall imaging. One of the first significant experiments in using a short range (tower or vehicle based) radar to estimate soil moisture was carried out in 1975 at the University of Kansas (See [16]). The data was collected from five sample fields using a truck mounted Microwave Active Spectrometer (MAS) system. In addition to measuring the dependence of backscatter data on soil moisture, the experiment established the dependence on parameters such as soil surface roughness, incidence angle and measurement frequency. The measurement frequencies were varied between 1 and 8 GHz so the penetration into the subsurface layers was limited. In [17] several ground penetrating radar systems for detecting buried or sunken objects are described. Most of these systems have transmit and receive antennas in contact or close proximity to the target, greatly reducing the footprint size and practicality for many applications. In [18] a tower based low frequency system operating at frequencies down to 137 MHz is used to estimate root-zone soil moisture.

1.3 Dissertation Contribution

The contributions of this dissertation span over a broad range of activities, including the development of forward and inverse scattering models, the design of radar systems and measurement techniques and the development of advanced radar data processing algorithms. The main contributions include:

• The development of an efficient forward scattering model for a three-layer medium.

• A versatile and efficient T-matrix method for cylinders with arbitrary cross sections.

• A robust inversion algorithm based on the conjugate gradient method.

• A new compact multifrequency radar system and advanced data processing algorithm.

An efficient forward scattering model based on EBCM and scattering matrix technique was developed for three layer media with non-smooth interfaces. The model with a periodic interface between the 1^{st} and 2^{nd} layers is more accurate and efficient than the one with both rough interfaces for a number of applications.

The three layer model is then extended by the inclusion of a cylinder with an arbitrary cross section inside the 3^{rd} layer. Such models are especially important in through-the-wall imaging and detection of buried objects. To incorporate the cylinder into the model, compact and efficient T-matrix equations were developed for both TM and TE polarizations and for metallic and dielectric cylinders.

The inversion algorithm presented in this dissertation is a robust local optimization algorithm based on the conjugate gradient method. Several important modifications were introduced to the standard conjugate gradient optimization to improve efficiency and accuracy of the algorithm. The numerical computation of the two gradient operations required in a conjugate gradient method is highly undesirable, and is one of the main sources of error and inefficiency of the standard optimization algorithm. To address this problem, the forward model is simulated over a large range of unknowns. The resultant data space is then broken into subspaces, and closed-form analytical

expressions are fitted to accurately model the function within each subspace. The conjugate gradient algorithm is applied to analytical expressions representing each subspace. The best solution is then chosen based on the magnitude of the cost function. As a result of the modification, all operations beyond obtaining closed-form expressions are analytical and do not accumulate error.

Another problem with retrieval algorithms is the number of unknowns. The computational cost of initial simulation, the cost of obtaining closed-form representations and the complexity of the inversion algorithm itself all increase rapidly with the number of unknowns. A significant efficiency improvement is achieved by sequential layer characterization. The model is first simulated at high frequency such that contributions of the subsurface can be safely neglected. The parameters pertaining to the first interface are retrieved and used in simulating the model at lower frequencies.

Even with these modifications, the number of parameters which go into a forward model is too great for efficient inversion. Most of these parameters, called ancillary parameters, are not the parameters of interest but nontheless are part of the forward scattering model. In this dissertation a careful analysis is performed on the sensitivity of the forward and inverse models to the errors in the ancillary parameters. The result of the analysis provides insights into the preferred way of obtaining these parameters (treating them as unknowns, direct measurement, approximation) and the accuracy with which they have to be obtained in order to achieve desirable inversion results.

To validate the models described in this dissertation and to further the technology of low frequency radar, a compact, tower-based radar was designed and manufactured. The radar is a multi-frequency bistatic pulse system that can measure changes in radar cross section corresponding to changes in the soil moisture measured by a co-located soil moisture sensor network. The instrument achieved 20 dB sensitivity improvement at approximately $\frac{1}{8}$ of the weight and $\frac{1}{5}$ of the deployment time compared to its predecessor. A coherent processing algorithm applied to the collected data allowed

for significant resolution and signal-to-noise ratio improvements.

1.4 Thesis Overview

The dissertation contains six chapters. Chapter 1 (this chapter) introduces the dissertation topic by discussing motivation and previous work done in the field. Chapter 2 introduces the forward scattering model for a three-layer medium with a periodic boundary between the 1^{st} and the 2^{nd} layers and a random rough boundary between the 2^{nd} and the 3^{rd} layers. The method is based on the Extended Boundary Condition Method and Scattering Matrix approach. The computational efficiency of the proposed forward model is analyzed, along with establishing the sensitivity of the model to the parameters of the subsurface layer. In Chapter 3 a forward scattering model is developed for a cylinder with an arbitrary cross section placed in the 3^{rd} layer of the medium. First, the T-matrix formulations are developed for the four main cases (TM PEC, TE PEC, TM Dielectic, TE Dielectric) and extensively validated for a number of special cases with analytical solutions. The derived T-matrix quantities are converted to scattering matrices, which are then combined with the relations developed in Chapter 2 to complete the formulation. In Chapter 4 an inversion algorithm for retrieval of parameters from scattering coefficients data for a three-layer medium is introduced. The algorithm uses a local optimizer based on the modified conjugate gradient method but differs from previous inverse algorithms by developing closed-form subspace-based representations of the forward model. The sensitivity of the algorithm to errors in scattering coefficients and ancillary parameters is explored. Chapter 5 is devoted to the discussion of a new tower based radar system. This compact, multi-frequency radar instrument was designed and built to validate forward and inverse scattering models. Instrument design, calibration, data collection and processing are described. In addition, the data from several measurement campaigns is discussed. The last chapter (Chapter 6) concludes the dissertation and discusses

future work.

CHAPTER II

Forward Scattering Model for Three-Layer Media with non-Smooth Interfaces

2.1 Introduction

In this chapter a forward scattering model for three layer media with non-smooth interfaces is introduced. The forward model is emphasized here because the forward and inverse models are inherently coupled such that in order to properly describe the inversion algorithm, adequate presentation of the forward model is essential. The forward model is based on the application of the Extended Boundary Condition Method to derive the scattering contributions from the top and the bottom interfaces. In Section 2.2 a set of scattering matrices for a single periodic interface is developed. A similar process is applied to the rough interface in Section 2.3. The plane wave modes of both interfaces are matched to produce the total scattering matrix for the entire system. The scattering matrix is then related to backscattering coefficients. The relative complexity of forward and inverse models associated with multi-layer structures developed in the past has often led to the use of simplified models that ignore the contributions of subsurface layers. In this chapter the effects of subsurface properties on the backscattering coefficients are explored in order to determine the extent of error due to ignoring the subsurface and the cases for which the use of

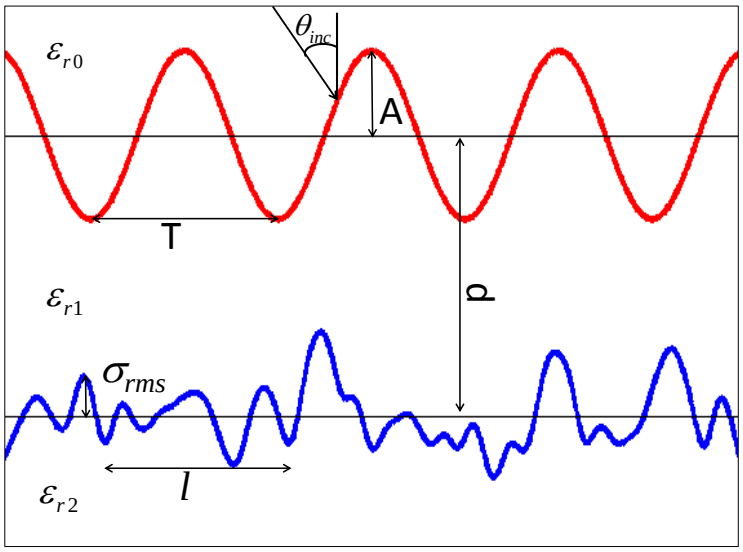

Figure 2.1: Geometric parameters for the problem. Surfaces are separated by distance d; ε_{r0}-ε_{r2} are relative dielectric constants, A and T are amplitude and period of a periodic surface, and σ_{rms} and l are RMS height and correlation length of a rough surface. Such surfaces are typical of fresh water and agricultural fields.

simplified models is justified.

The geometry of interest is a three layer medium with a periodic interface between the first and second layers and a rough interface between the second and third layers, as shown in Figure 2.1. This geometry occurs frequently in natural and man-made structures (See [19]). Lakes and rivers often have this cross-section, with the periodic top surface being representative of waves and the rough bottom surface representative of the lake or river beds. Plowed agricultural fields are another example of periodic-over-rough cross-section geometries, in which there is often a rough interface below the top periodic surface, where transition between sandy and clay soils occurs. The first layer is typically air, i.e., a homogeneous dielectric with the relative dielectric constant of one. The 2^{nd} and 3^{rd} layers are also modeled as homogeneous layers with relative dielectric constants ε_{r1} and ε_{r2}, which are in general complex. Figure 2.1 depicts the relevant parameters for the problem: amplitude A and period T for the periodic surface, RMS height σ_{rms} and correlation length l for the rough surface,

layer separation d, dielectric constants ε_{r0}, ε_{r1}, ε_{r2}, incidence angle θ_{inc}, and wave polarization.

The penetrating abilities of low frequency electromagnetic radiation make it a good candidate for this group of applications, provided sufficient resolution can be achieved, and a diversity of measurements (such as multiple polarizations) are available to provide sufficient independent information for retrieval of the several unknowns. In particular, multipolarization radar systems at L-band (∼1.2 GHz) and lower frequencies are well suited for this purpose. Through the use of accurate and efficient forward and inverse scattering model techniques, these radar measurements can be converted into estimates of the sought-after parameters of the surface and subsurface media.

2.2 Scattering Matrices of a Single Periodic Surface

The derivation of scattering from a single 1-D periodic surface is presented in [20]. In this work, the derivation for horizontal polarization (TE waves) is provided. The vertical polarization solution (TM waves) can be obtained using duality. If we consider a periodic surface described with variations only in the x-direction, the surface height profile can be described by $f(x) = f(x + L)$, where L is the period of the surface. The incident electric field can be expressed as:

$$E_i = \hat{y} E_0 e^{ik_i r}, \quad \text{where} \tag{2.1}$$

$$k_i = \hat{x} k_{ix} - \hat{z} k_{iz} \tag{2.2}$$

Using the scalar form of the Huygens' principle and extinction theorem for the upper half-space, the electric field above and below the periodic interface can be written as:

$$E_{iy}(r) - \int_{-\infty}^{+\infty} dl\{g_0(r,r')\hat{n}\cdot\nabla_s' E_{0y}(r') - E_{0y}(r')\hat{n}\cdot\nabla_s' g_0(r,r')\} = \begin{cases} E_{0y}(r) & z > f(x) \\ 0 & z < f(x) \end{cases} \tag{2.3}$$

where dl is the differential unit of length along the surface and r, r' are vectors from the origin to the observer and the source. Repeating for the lower half-space:

$$\int_{-\infty}^{+\infty} dl\{g_1(r,r')\hat{n}\cdot\nabla_s' E_{1y}(r') - E_{1y}(r')\hat{n}\cdot\nabla_s' g_1(r,r')\} = \begin{cases} 0 & z > f(x) \\ E_{1y}(r) & z < f(x) \end{cases} \tag{2.4}$$

The two-dimensional Green's function can be expressed as

$$g_t(r,r') = \frac{i}{4}H_0^1(k_{tr}|r-r'|) = \frac{i}{4\pi}\int_{-\infty}^{+\infty}\frac{1}{k_{tz}}e^{i(k_x(x-x')+k_{tz}|z-z'|)}dk_x \tag{2.5}$$

Equations 2.3 and 2.4 are over an infinite domain and therefore not fit for numerical solutions. The integrals in equations 2.3 and 2.4 can be represented as infinite summations of integrals over one period:

$$E_{ty}(r) = (-1)^{t+1}\sum_{n=-\infty}^{n=+\infty}\int_{x_0+nL}^{x_0+(n+1)L} dl\{g_t(r,r')\hat{n}\cdot\nabla_s' E_{ty}(r') - E_{ty}(r')\hat{n}\cdot g_t(r,r')\}, \tag{2.6}$$

where $t = 0$ and $t = 1$ represent upper and lower half-spaces respectively.

Since the surface only varies in the x-dimension with periodicity L, according to the Floquet theorem, all field quantities must be periodic and differ only by a phase factor.

$$E(x+L,y,z) = E(x,y,z)e^{ik_xL} \tag{2.7}$$

As a result, Equation 2.6 can be expressed as an integral over only one period using the periodic Green's function (see [21] for more detail):

$$g_t(r,r') = \frac{i}{4}\sum_{n=-\infty}^{n=+\infty} H_0^1\Big(k_{tr}\sqrt{(x-x'-nL)^2+(z-z')^2}\Big)e^{ik_{xi}nL} \tag{2.8}$$

The rate of convergence of the periodic Green's function is very slow and therefore it is not fit for numerical computation. Using a Fourier transform identity equation 2.8 can be tranformed to

$$g_t(r,r') = \frac{i}{2L}\sum_{n=-\infty}^{n=+\infty} \frac{1}{k_{tnz}} e^{ik_{nx}(x-x')}e^{ik_{tnz}|z-z'|}, \tag{2.9}$$

where k_{nx} and k_{tnz} are given by:

$$k_{nx} = k_{xi} + \frac{2\pi n}{L}, \qquad\qquad k_{tnz} = \sqrt{k_t^2 - k_{nx}^2} \tag{2.10}$$

The transformed Green's function can be interpreted as a field produced by a periodic array of line currents of progressive phase. This array produces a finite number of propagating modes (called Floquet modes). A mode is propagating when the expression under the radical for k_{tnz} is positive and evanescent if it is negative. Evanescent modes decay exponentially away from the interface. The number of propagating modes is determined by the period-over-wavelength ratio and the incidence angle. We define quantities f_{min} and f_{max} to be the minimum and the maximum extent of the periodic surface respectively. By allowing z to be larger than f_{max} or smaller than f_{min}, $|z-z'| = z-z'$ for $z > f_{max}$, and $|z-z'| = -(z-z')$ for $z < f_{min}$. Substituting the transformed periodic Green's function into the field equations produces field equations above and below the periodic interface.

The result of applying the extinction theorem above the interface (region 0) is:

$$E_{0y}(r) = E_{iy}(r) + \sum_{n=-\infty}^{n=+\infty} b_{01n} e^{i(k_{nx}x + k_{0nz}z)}, z > f_{max} \tag{2.11a}$$

$$0 = E_{iy}(r) + \sum_{n=-\infty}^{n=+\infty} a_{01n} e^{i(k_{nx}x - k_{0nz}z)}, z < f_{min} \tag{2.11b}$$

The result of applying the extinction theorem below the interface (region 1) is:

$$E_{1y}(r) = \sum_{n=-\infty}^{n=+\infty} b_{11n} e^{i(k_{nx}x + k_{1nz}z)}, z > f_{max} \tag{2.12a}$$

$$0 = \sum_{n=-\infty}^{n=+\infty} a_{11n} e^{i(k_{nx}x - k_{1nz}z)}, z < f_{min} \tag{2.12b}$$

where coefficients b_{t1n} and a_{t1n} are given by

$$b_{t1n} = \frac{-i}{2Lk_{tnz}} \int \{\hat{n} \cdot \nabla E_{ty}(r') e^{-i(k_{nx}x' + k_{tnz}z')} - E_{ty}(r') \hat{n} \cdot \nabla e^{-i(k_{nx}x' + k_{tnz}z')}\} dl \tag{2.13}$$

$$a_{t1n} = \frac{-i}{2Lk_{tnz}} \int \{\hat{n} \cdot \nabla E_{ty}(r') e^{-i(k_{nx}x' - k_{tnz}z')} - E_{ty}(r') \hat{n} \cdot \nabla e^{-i(k_{nx}x' - k_{tnz}z')}\} dl \tag{2.14}$$

The surface fields can be expanded in terms of their Fourier series

$$E_{1y}(x, f(x)) = \sum_{m=-\infty}^{m=+\infty} \beta_m e^{ik_{mx}x} \tag{2.15}$$

$$dl\hat{n} \cdot \nabla E_{1y}(x, f(x)) = \sum_{m=-\infty}^{m=+\infty} \gamma_m e^{ik_{mx}x} \tag{2.16}$$

The incident field can be decomposed into Floquet modes as well as producing a vector with a sole non-zero entry corresponding to $n = 0$. By substituting Equations 2.13-2.16 into the field expressions given by Equations 2.11a-2.12b and imposing boundary

conditions, the result can be cast into infinite summations

$$\sum_{m=-\infty}^{m=+\infty} U_{nm}^{1+}\beta_m + U_{nm}^{2+}\gamma_m = a_{01n} \tag{2.17a}$$

$$\sum_{m=-\infty}^{m=+\infty} Q_{nm}^{2-}\beta_m + Q_{nm}^{1-}\gamma_m = 0 \tag{2.17b}$$

In Equation 2.17a, a_{01n} is a Floquet expansion of the incident field. The infinite summations are truncated to produce matrix equations for β and γ,

$$\begin{bmatrix} \beta \\ \gamma \end{bmatrix} = \begin{bmatrix} \overline{\overline{U}}^{1+} & \overline{\overline{U}}^{2+} \\ \overline{\overline{Q}}^{2-} & \overline{\overline{Q}}^{1-} \end{bmatrix}^{-1} \begin{bmatrix} a_{01n} \\ 0 \end{bmatrix} \tag{2.18}$$

Similarly, the upward and downward propagating field amplitudes can be expressed via similar matrix equations:

$$-\begin{bmatrix} \overline{\overline{U}}^{1-} & \overline{\overline{U}}^{2-} \\ \overline{\overline{Q}}^{2+} & \overline{\overline{Q}}^{1+} \end{bmatrix} \begin{bmatrix} \beta \\ \gamma \end{bmatrix} = \begin{bmatrix} b \\ A \end{bmatrix} \tag{2.19}$$

Substituting Equation 2.18 into Equation 2.19 leads to

$$\begin{bmatrix} b \\ A \end{bmatrix} = -\begin{bmatrix} \overline{\overline{U}}^{1-} & \overline{\overline{U}}^{2-} \\ \overline{\overline{Q}}^{2+} & \overline{\overline{Q}}^{1+} \end{bmatrix} \begin{bmatrix} \overline{\overline{U}}^{1+} & \overline{\overline{U}}^{2+} \\ \overline{\overline{Q}}^{2-} & \overline{\overline{Q}}^{1-} \end{bmatrix}^{-1} \begin{bmatrix} a_{01n} \\ 0 \end{bmatrix} \tag{2.20}$$

The Scattering matrix relates amplitudes of the incident wave to those of the reflected and transmitted waves

$$\begin{bmatrix} R & \tilde{T} \\ T & \tilde{R} \end{bmatrix} = -\begin{bmatrix} \overline{\overline{U}}^{1-} & \overline{\overline{U}}^{2-} \\ \overline{\overline{Q}}^{2+} & \overline{\overline{Q}}^{1+} \end{bmatrix} \begin{bmatrix} \overline{\overline{U}}^{1+} & \overline{\overline{U}}^{2+} \\ \overline{\overline{Q}}^{2-} & \overline{\overline{Q}}^{1-} \end{bmatrix}^{-1} \tag{2.21}$$

with R and T standing for the reflection and transmission matrices looking down and

$\tilde{R}$ and $\tilde{T}$ looking up. The $\overline{\overline{U}}$ and $\overline{\overline{Q}}$ matrices are given by

$$U_{nm}^{1\pm} = \frac{k_{nx}k_{mx} - k_0^2}{2Lk_{0nz}} I_0^{\pm},\ U_{nm}^{2\pm} = \frac{-i}{2Lk_{0nz}} \frac{k_0}{k_1} \frac{Y_1}{Y_0} I_0^{\pm} \tag{2.22}$$

$$Q_{nm}^{1\pm} = \frac{k_{nx}k_{mx} - k_1^2}{2Lk_{1nz}} I_1^{\pm},\ Q_{nm}^{2\pm} = \frac{-i}{2Lk_{1nz}} I_1^{\pm}, \tag{2.23}$$

where $I_0^{\pm}$ and $I_1^{\pm}$ are given by:

$$I_0^{\pm} = \int_0^L e^{i(2\pi(m-n)\frac{x'}{L} \pm k_{0nz} f(x'))}\, \mathrm{d}x' \tag{2.24}$$

$$I_1^{\pm} = \int_0^L e^{i(2\pi(m-n)\frac{x'}{L} \pm k_{1nz} f(x'))}\, \mathrm{d}x' \tag{2.25}$$

Special care is needed to properly and efficiently evaluate the I integrals. A direct numerical integration requires four $(I_0^-, I_0^+, I_1^-, I_1^+)$ integral evaluations for every matrix entry, for a total of $16N^2 + 16N + 4$ integral evaluations where N is the number of Floquet modes. Moreover, for large values of k_{tnz} the integrand oscillates rapidly requiring a very fine discretization. These problems render direct integral evaluation impractical. An alternative method formulated in [22] relies on the Fast Fourier Transform algorithm and allows for orders of magnitude improvement in computational efficiency. The I integrals generally take the form of

$$I(\tau) = \int_0^L e^{i2\pi\tau\frac{x'}{L}} e^{ik(\tau)f(x')} dx' \tag{2.26}$$

and can be rewritten as follows:

$$I(\tau) = \delta(\tau) + K(\tau) = \delta(\tau) + \int_0^L e^{i2\pi\tau\frac{x'}{L}} (e^{ik(\tau)f(x')} - 1) dx' \tag{2.27}$$

Next, $K(\tau)$ can be evaluated by expanding it using a Taylor series and integrating the result term by term

$$K(\tau) = \sum_{n=1}^{N} \frac{(ik(\tau))^n}{n!} C(\tau, n) \tag{2.28}$$

$$C(\tau, n) = \int_0^L e^{i2\pi\tau \frac{x'}{L}} f^n(x') dx' = \frac{1}{M} fft(f^n(x'_d), M) \tag{2.29}$$

where $f(x_d)$ is a vector of length M of discrete samples of a continuous function $f(x)$. The efficiency of the algorithm is further improved if the number of points of the surface is equal to a power of 2.

2.3 Cross Section Coefficients of the Three-Layer Medium

After the scattering matrices for a single periodic interface are obtained, the process is repeated for the rough interface. Then, the modes for periodic and rough surface are matched to obtain a total reflection matrix for the three-layer system. Finally, scattering coefficients are computed from the total reflection matrix.

2.3.1 Scattering Matrices of a Single Rough Surface

Although a random rough surface is not periodic, the EBCM algorithm for periodic surfaces can still be applied provided that the surface statistics can be properly captured. The two parameters that generally describe a 1-D random rough surface are the surface roughness σ_{rms} and correlation length l. Surface roughness is computed by $\sigma_{rms} = \sqrt{\frac{1}{N}\sum_{n=1}^{N}(x_n - \overline{x})^2}$, where $\overline{x}$ is the mean value for the surface. Correlation length is a distance from a point on the surface required for the autocorrelation coefficient to drop to $\frac{1}{e}$. Figures 2.2 and 2.3 demonstrate the impact of correlation

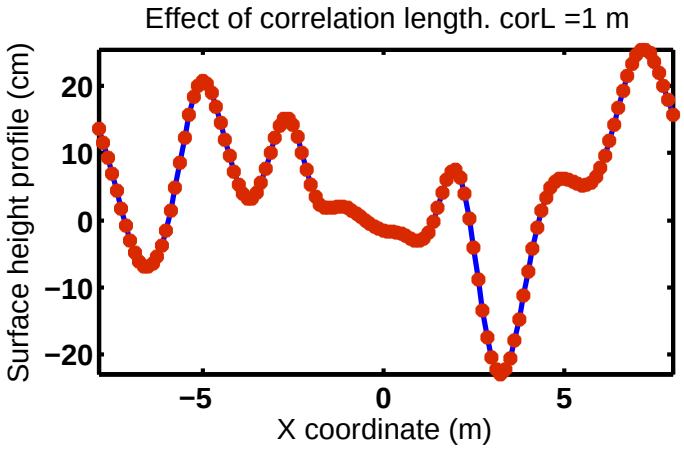

Figure 2.2: Random rough surface with long correlation length. The effect of correlation length on the rough surface height profile. The surface is a random rough surfaces with $\sigma_{rms} = 10cm$. The correlation length of the surface is 1 m

length parameter on the rough surface profile. Rough surfaces that have a short correlation length feature rapid slope variation while surfaces with longer correlation lengths have a gradual variation. Since the surface profile is not deterministic, many surface realizations are necessary to adequately capture the surface statistics.

2.3.2 Generalized Scattering Matrix of the Three-Layer Medium

Once scattering matrices for the periodic and rough surfaces are computed, the results are cascaded to form a generalized scattering matrix for the entire system. The total reflection matrix for the entire system is given by

$$[R_t] = [R_1] + [\tilde{T}_1][\phi][R_2]([I] - [\phi][\tilde{R}_1][\phi][R_2])^{-1}[\phi][T_1] \tag{2.30}$$

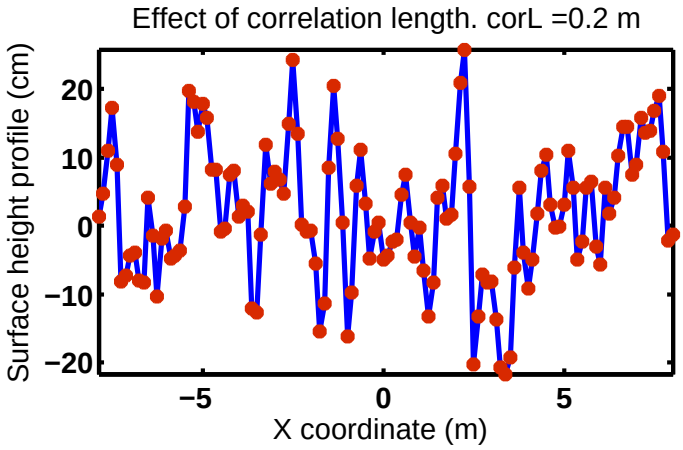

Figure 2.3: Random rough surface with short correlation length. The effect of correlation length on the rough surface height profile. The surface is a random rough surfaces with $\sigma_{rms} = 10cm$. The correlation length of the surface is 20 cm

where subscripts 1 and 2 represent 1^{st} and 2^{nd} interfaces respectively, I is the identity matrix and $[\phi]$ is a phase shifting matrix and is given by:

$$[\phi] = \begin{bmatrix} e^{ikd\cos\phi_1} & \cdots & 0 \\ \vdots & \ddots & \vdots \\ 0 & \cdots & e^{ikd\cos\phi_n} \end{bmatrix} \tag{2.31}$$

In Equation 2.31, k corresponds to the propagation constant in the medium between periodic and rough interfaces and ϕ_n is the propagation direction of the n^{th} Floquet mode in the middle layer. If both surfaces are completely flat (both the amplitude of the periodic interface and roughness of the rough interface are equal to zero) and the dielectric constant of the 3^{rd} layer is the same as the dielectric constant of the first layer, the expression for the total reflection matrix simplifies to the familiar equation for the reflection coefficient from a homogeneous dielectric slab. Equation 2.30 can be recursively extended to N layers. All the multiple scattering interactions are incorporated in the inverse term. The advantage of this method becomes especially apparent when performing the sensitivity analysis to a certain parameter since only

the matrix containing the parameter in question would need to be recomputed. To properly match the modes of the periodic interface with the modes of the rough interface, the periods of both surfaces have to be equal. Since the artificial period of the rough surface needs to be many correlation lengths long to properly capture the surface statistics, it is typically larger than the natural period of the periodic surface. Since any periodic function of period T is also periodic with period nT, an artificial period for both surfaces is chosen in such a way that it is an integer multiple of the period of the periodic surface and is large enough to properly capture the statistics of the rough surface.

2.3.3 RCS of the Three-Layer Medium

Once a total reflection matrix for the system is obtained, radar scattering coefficients can be computed as follows (See [23]):

$$\sigma_{2D} = L_\lambda \cos^2 \theta_s |b_m|^2 \tag{2.32}$$

where L_λ is the artificial period of both periodic and rough surfaces normalized by the wavelength, $[b] = [R_t][A]$, and [A] is a column vector containing the incident field coefficients. The model is validated for several special cases with the SPM (See [6]).

2.4 Computational Efficiency and Sensitivity to Subsurface

2.4.1 Computational Efficiency

Table 2.1 compares computational efficiencies of the MOM and EBCM methods. Special care is needed to address the differences in the type of metrices used to assess computational efficiency of the different numerical models. In the case of Method of Moments (MOM), unknowns represent induced current elements on a surface of a scattering target and therefore have to be densely discretized to preserve

Table 2.1: Computational efficiency comparison between EBCM and MOM. The surfaces are 40 λ long.

EBCM	MOM
modes = 101	segments = 800
interfaces = 2	interfaces = 2
seconds/realization = .91	seconds/realization = 117

the accuracy of the model. Generally, it is recommended to have at least 10 unknowns per wavelength. In the case of EBCM, modes represent discrete scattering directions and therefore usually many fewer modes than MOM segments suffice. EBCM becomes even more computationally advantageous as compared to MOM when applied to multilayer problems since scattering matrices are developed independently for each interface and then cascaded using only a few multiplications.

2.4.2 Sensitivity to Subsurface Parameters

There is great interest in the Earth Science community to map soil moisture on a global scale. In most cases the air/soil system is modeled as two homogeneous dielectric layers separated by a rough interface. Such models ignore the effects of subsurface interfaces that are often present in reality. Soils, particularly croplands, can often be considered periodic interfaces with a small roughness on top and a rough interface between the top layer of soil and the subsurface layer (for example bedrock). It is therefore important to investigate cases when the effects of the 2nd interface are significant and when they can be neglected. There are several key parameters that are especially significant: depth of the subsurface layer, difference in soil composition and water content (dielectric contrast) between the layers, roughness (and periodic properties) of top and bottom interfaces, attenuation loss in the middle layer, and measurement frequency.

Figure 2.4 shows the effect of the depth of the 2^{nd} interface. In this case, the medium under the first interface is not very lossy ($\epsilon_{r1} = 5.5 + i$); therefore, there

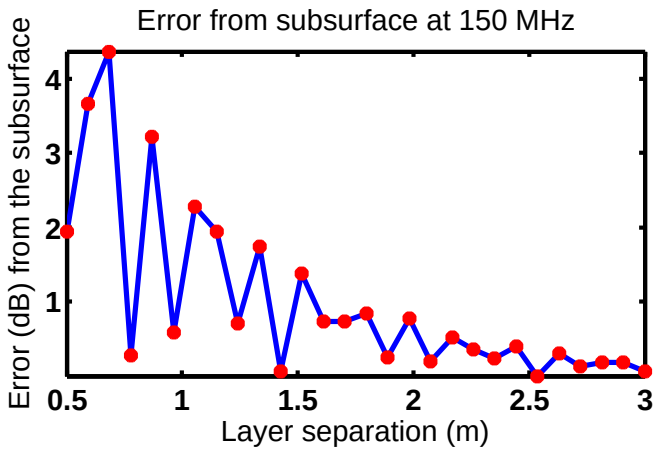

Figure 2.4: Error in RCS as a function of layer separation: VHF case. At low frequencies and low losses below the first interface errors from ignoring the subsurface can be significant. The error variation with the depth of the 2^{nd} interface clearly displays underdamped characteristics. Simulation parameters: frequency $= 150MHz$, Amplitude $= 3.5cm$, period $=2m$, $\epsilon_{r1} = 5.5 + i$, $\epsilon_{r2} = 35 + 2i$, $\sigma_{rms1} = 2cm$, $l_1 = 20cm$, $\sigma_{rms2} = 5cm$, $l_2 = 20cm$

is a clear oscillatory pattern in the error with the envelope of the error gradually getting smaller (due to loss). The error can be even more significant if the roughness in the interface between the 2^{nd} and 3^{rd} layers is large (see Figure 2.6). If the losses are small and the 2^{nd} interface is close to the top surface, the modeling errors can be unacceptably large if the subsurface is not included in the scattering model. At higher frequencies, the effects of the subsurface rapidly diminish. This fact makes low frequencies very attractive when characterizing the subsurface properties. Figure 2.5 shows the error in predictions of backscattering cross section as a function of layer separation for L-band. At higher frequencies the effect of the subsurface is only significant when the 2^{nd} interface is shallow.

2.4.3 Chapter Conclusion

In this chapter an efficient forward scattering model based on Extended Boundary Condition Method was presented. Unlike many of the previous works employing forward models based on EBCM [6] and modelling the system as two rough inter-

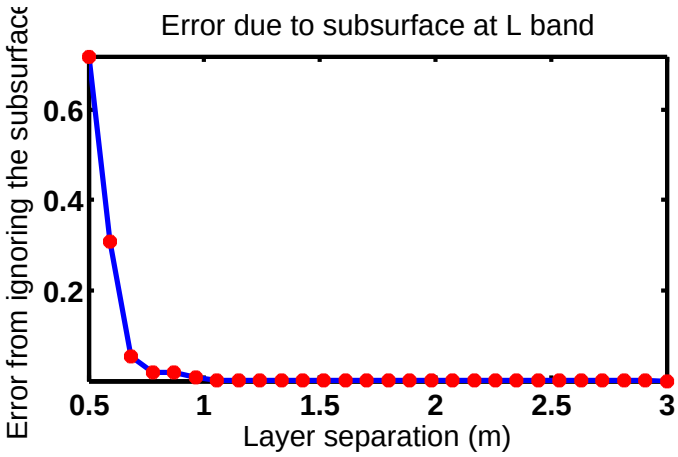

Figure 2.5: Error in RCS as a function of layer separation: L band case. At higher frequencies error variation displays overdamped characteristics. Simulation parameters: frequency = $1150MHz$, Amplitude = $3.5cm$, period =$2m$, $\epsilon_{r1} = 5.5 + i$, $\epsilon_{r2} = 35 + 2i$, $\sigma_{rms1} = 2cm$, $l_1 = 20cm$, $\sigma_{rms2} = 5cm$, $l_2 = 20cm$

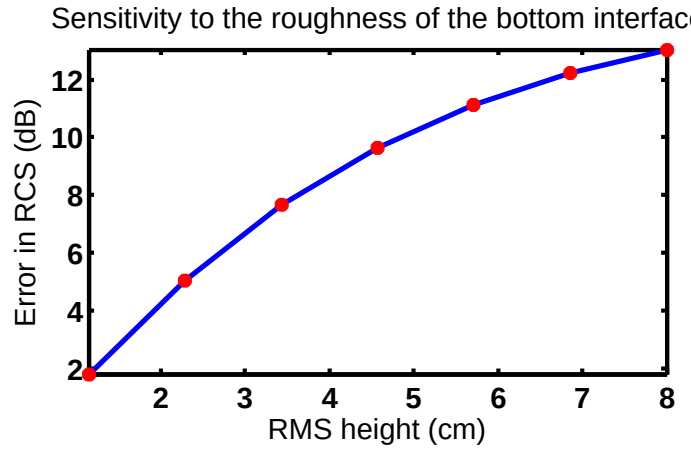

Figure 2.6: Error in RCS as a function of surface roughness σ_{rms}. Larger values of roughness of the 2^{nd} interface has a greater impact on the total RCS. Simulation parameters: frequency = $150MHz$, Amplitude = $3.5cm$, period =$2m$, $\epsilon_{r1} = 5.5 + i$, $\epsilon_{r2} = 35 + 2i$, $\sigma_{rms1} = 2cm$, $l_1 = 20cm$, $l_2 = 20cm$

faces, the top interface in this work is modeled as a periodic interface. Many natually occuring and anthropogenic landscapes are more accurately modeled as periodic interfaces on top of a rough interface. In addition to a more accurate modelling, since periodic interfaces are deterministic, there is no need to generate multiple realizations of the surface, which significantly improves computational efficiency. In this chapter

the computational efficiency of the presented forward model is compared to an established numerical technique. Also, since many existing scattering models of the soil completely discount contributions from the subsurface layers, this chapter analyzed the errors that result from such approximations for several cases.

CHAPTER III

Scattering from an Arbitrary Cylinder Behind a non-Smooth Wall

3.1 Introduction

In this chapter an efficient forward scattering model is developed for a $2-D$ cylinder with an arbitrary cross section behind a non-smooth wall or under a non-smooth surface. Since the development of the T-matrix technique for a single scatterer by Waterman [7] in the early 1960s, the approach found many applications especially in multiple scattering problems. T-matrix is convenient since it does not depend on the incidence angle or the location of the object thereby reducing the number of parameters to the properties of the object and the polarization of the incoming radiation. In many multiple scattering problems such as detection of objects behind an obstacle, through-the-wall imaging, etc., real world objects have often been approximated as circular cylinders [8]. The analytical expressions for a T-matrix of a circular cylinder are simple and widely reported but cannot adequately describe a scatterer with noncircular cross section; therefore a more versatile T-matrix method is needed. In [11] the solution for obtaining a T-matrix for the simplest case of a PEC cylinder for TM polarization is presented. However, the solution for dielectric cylinders and TE PEC case have not been previously developed. In this chapter, explicit expressions

are derived relating the T-matrix with an impedance matrix obtained by MOM for both PEC and Dielectric cylinders for both polarizations. The results are extensively validated for special cases against analytical models. Also, the sensitivity of scattering coefficients to the shape of the cylinder is explored by comparing the response of arbitrary cylinders with the response of the circular cylinder for all four cases. Once the expressions for the T-matrices are derived, the results are transformed into R-matrices. The resulting R-matrices are then cascaded with the scattering matrices for periodic or rough interfaces to obtain a scattering matrix for the entire system.

3.2 T matrices of PEC and dielectic cylinders for TM and TE polarizations

3.2.1 TM PEC

For a normally incident TM wave, the only current component induced on an infinite conducting cylinder is J_z and the scattered field can be expressed as:

$$E_z^{sc} = ik\eta A_z(t) \tag{3.1}$$

where

$$A_z(t) = \int J_z(t^{'})\frac{i}{4}H_0^1(kR)dt^{'} \tag{3.2}$$

$$R = \sqrt{\Big(x(t) - x(t^{'})\Big)^2 + \Big(y(t) - y(t^{'})\Big)^2} \tag{3.3}$$

Imposing the boundary conditions on the surface of the scatterer makes the total electric field vanish and the incident field equal to the negative of the scattered field. Applying a standard Method of Moments method (MOM) [24] by discretizing the cylinder into M segments, the following approximate matrix equation is obtained:

$$\begin{bmatrix} E_z^{inc}(t_1) \\ \vdots \\ E_z^{inc}(t_M) \end{bmatrix} = \begin{bmatrix} Z_{11} & \dots & Z_{1M} \\ \vdots & \ddots & \vdots \\ Z_{M1} & \dots & Z_{MM} \end{bmatrix} \begin{bmatrix} j_1 \\ \vdots \\ j_M \end{bmatrix} \tag{3.4}$$

The elements of impedance matrix Z are given by:

$$Z_{mm} = \frac{k\eta w_m}{4}\left\{1 + i\frac{2}{\pi}\left[ln\left(\frac{\gamma k w_m}{4}\right)\right]\right\}, \quad m = n \tag{3.5}$$

$$Z_{mn} = \frac{k\eta w_m}{4} H_0^1(kR_{mn}), \qquad m \neq n \tag{3.6}$$

$$R_{mn} = \sqrt{(x_m - x_n)^2 + (y_m - y_n)^2} \tag{3.7}$$

In Equation 3.5, w_m is the width of the m^{th} segment and γ is a constant approximately equal to 1.78107. The scattered field can now be represented as a sum of the individual contributions from each induced current element:

$$E_z^s = -\frac{k\eta}{4}\sum_{m=1}^{M} j_m H_0^1(k|\rho - \rho_m|), \tag{3.8}$$

where $R = |\rho - \rho_m|$, with ρ being a vector between the origin and an observer and ρ_m a vector between the origin and the m^{th} segment. Using the Addition theorem for cylindrical harmonics, $H_0^1(k|\rho - \rho_m|)$ can be expressed as an infinite sum:

$$H_0^1(k|\rho - \rho_m|) = \sum_{n=-\infty}^{\infty} J_n(k\rho_m)e^{-in\phi_m} H_n^1(k\rho)e^{in\phi} \tag{3.9}$$

Truncating the infinite summations at N, Equation 3.8 can be cast into a matrix

equation:

$$E_z^s = -\frac{k\eta}{4}[\ \ldots H_n^1(k\rho)e^{in\phi}\ldots\ ]P^p \begin{bmatrix} \vdots \\ j_m \\ \vdots \end{bmatrix},\ where \tag{3.10}$$

P^p is an $2N+1$ by M matrix whose entries are given by:

$$P_{nm}^p = J_n(k\rho_m)e^{-in\phi_m} \tag{3.11}$$

The current density vector can be expressed as a product of an inverse of an impedance matrix and an incident field vector $J = Z^{-1}E^{inc}$. Expanding E^{inc} in terms of harmonics and truncating infinite summations, the current density can be expressed as $J = Z^{-1}P$, where

$$P_{mn} = J_n(k\rho_m)e^{in\phi_m} \tag{3.12}$$

It is clear that P^p is a conjugate transpose of matrix P. Substituting the expression for J into Equation 3.10 produces the expression for the T-matrix of a perfectly conducting cylinder for TM polarization.

$$T = -\frac{k\eta}{4}P^\dagger Z^{-1}P \tag{3.13}$$

3.2.2 TE PEC

The derivation of a T-matrix for TE-PEC case is more complicated and requires several more steps due to the partial derivatives present in the expression of the scattered magnetic field. The equation for the scattered magnetic field can be simplified to:

$$H_z^s = \frac{\partial A_y}{\partial x} - \frac{\partial A_x}{\partial y} \tag{3.14}$$

where A is given by:

$$A(t) = \int \hat{t}(t^{'}) J_t(t^{'}) \frac{i}{4} H_0^1(kR) dt^{'} \tag{3.15}$$

$$\hat{t}(t) = \hat{x} \cos \Omega(t) + \hat{y} \sin \Omega(t) \tag{3.16}$$

where Ω represents orientation of each segment with respect to x axis. A_x and A_y, the components of the magnetic vector potential, become:

$$A_x(t) = \int \cos \Omega(t^{'}) J_t(t^{'}) \frac{i}{4} H_0^1(kR) dt^{'} \tag{3.17}$$

$$A_y(t) = \int \sin \Omega(t^{'}) J_t(t^{'}) \frac{i}{4} H_0^1(kR) dt^{'} \tag{3.18}$$

Following a similar procedure to the TM-PEC case but applying boundary conditions for the magnetic field, the equations for the elements of the impedance matrix can be derived. Off-diagonal matrix entries are given by:

$$Z_{mn} = \frac{-ikw_m}{4} (\sin \Omega_n \frac{x_m - x_n}{R_{mn}} - \cos \Omega_n \frac{y_m - y_n}{R_{mn}}) H_1^1(kR_{mn}) \tag{3.19}$$

$$R_{mn} = \sqrt{(x_m - x_n)^2 + (y_m - y_n)^2} \tag{3.20}$$

Diagonal entries are approximately equal to:

$$Z_{mm} = \frac{1}{2} \tag{3.21}$$

Integrals in Equations 3.17 and 3.18 can be approximated by summations before partial derivatives are computed:

$$\frac{\partial A_x}{\partial y} = -\sum_{m=1}^{M} \frac{ikw_m}{4} \cos \Omega_m \sin \phi^{''} J_m H_1^1(kR) \tag{3.22}$$

$$\frac{\partial A_y}{\partial x} = -\sum_{m=1}^{M} \frac{ikw_m}{4} \sin\Omega_m \cos\phi'' J_m H_1^1(kR) \tag{3.23}$$

Note that $\sin\phi''$ and $\cos\phi''$ can be written as:

$$\cos\phi'' = \frac{1}{2}(e^{i\phi''} + e^{-i\phi''}); \;\; \sin\phi'' = \frac{1}{2i}(e^{i\phi''} - e^{-i\phi''}) \tag{3.24}$$

Substituting Equation 3.24 into Equations 3.22 and 3.23, we obtain an expression for the scattered field H_z^s:

$$\begin{aligned} H_z^s = &-\sum_{m=1}^{M} \tfrac{ikw_m}{8} \sin\Omega_m (e^{i\phi''} + e^{-i\phi''}) J_m H_1^1(kR) \\ &-\sum_{m=1}^{M} \tfrac{kw_m}{8} \cos\Omega_m (e^{i\phi''} - e^{-i\phi''}) J_m H_1^1(kR) \end{aligned} \tag{3.25}$$

Following a few more manipulations, the scattered magnetic field can be expressed as:

$$\begin{aligned} H_z^s = \;\; -\sum_{m=1}^{M} \tfrac{kw_m}{8} J_m \Big(& e^{i\phi''} H_1^1(kR) e^{-i\Omega_m} + \\ & e^{-i\phi''} H_{-1}^1(kR) e^{i\Omega_m} \Big) \end{aligned} \tag{3.26}$$

The Addition theorem for cylindrical harmonics can be expressed as:

$$H_{\pm 1}(k_\rho |\rho - \rho'|) e^{\pm i\phi''} = \sum_{n=-\infty}^{\infty} J_{n\mp 1}(k_\rho \rho') H_n(k_\rho \rho) e^{in\phi} e^{-i(n\mp 1)\phi'} \tag{3.27}$$

Applying the Addition theorem to Equation 3.26 and truncating the infinite summation, two matrixes P^+ and P^- are defined as:

$$P_{nm}^{+} = J_{n-1}(k_\rho \rho_m) e^{-i(n-1)\phi_m} e^{-i\Omega_m} \tag{3.28}$$

$$P_{nm}^{-} = J_{n+1}(k_\rho \rho_m) e^{-i(n+1)\phi_m} e^{i\Omega_m} \tag{3.29}$$

Following a similar procedure as for TM-PEC case and expressing the induced current density vector as a product of the inverse of the impedance matrix and incident

magnetic field, a T-matrix for TE PEC can be written as:

$$T = -\frac{kw_m}{8}(P^+ + P^-)Z^{-1}P. \tag{3.30}$$

3.2.3 TM Dielectric

In the case of scattering from a dielectric cylinder for TM polarization the electric field can be expressed as:

$$E_z^s = ik\eta A_z - \frac{\partial F_y}{\partial x} + \frac{\partial F_x}{\partial y}, \tag{3.31}$$

where A_z and F are given by:

$$A_z = \int J_z(t^{'})\frac{i}{4}H_0^1(kR)dt^{'} \tag{3.32}$$

$$F = \int \hat{t}(t^{'})K_t(t^{'})\frac{i}{4}H_0^1(kR)dt^{'} \tag{3.33}$$

Enforcing boundary conditions at an infinitesimal distance outside and then inside the cylinder surface produces a pair of coupled equations which upon discretization and pulse basis testing produce a 2 x 2 matrix structure given by:

$$\begin{bmatrix} E \\ 0 \end{bmatrix} = \begin{bmatrix} A & B \\ C & D \end{bmatrix} \begin{bmatrix} J \\ K \end{bmatrix} \tag{3.34}$$

In Equation 3.34, A, B, C, D are M by M matrices and J, K are M by 1 electric and magnetic current density vectors. The definition of elements of matrices A and C is very similar to the TM-PEC case with the exception that in the case of matrix C, k_0 and η_0 are replaced with k_d and η_d, which are the wave number and impedance inside the dielectric. Similarly, B and D matrix entries are similar to impedance matrix

entries for the TE-PEC case. Off-diagonal matrix entries are represented by:

$$
\begin{aligned}
A_{mn} &= \tfrac{k_0\eta_0 w_m}{4} H_0^1(k_0 R_{mn}) \\
C_{mn} &= \tfrac{k_d\eta_d w_m}{4} H_0^1(k_d R_{mn})
\end{aligned}
$$

$$
\begin{aligned}
B_{mn} = \tfrac{ik_0 w_m}{4}(\sin\Omega_n \tfrac{x_m - x_n}{R_{mn}} - \\
\cos\Omega_n \tfrac{y_m - y_n}{R_{mn}}) H_1^1(k_0 R_{mn})
\end{aligned}
\tag{3.35}
$$

$$
\begin{aligned}
D_{mn} = \tfrac{ik_d w_m}{4}(\sin\Omega_n \tfrac{x_m - x_n}{R_{mn}} - \\
\cos\Omega_n \tfrac{y_m - y_n}{R_{mn}}) H_1^1(k_d R_{mn})
\end{aligned}
$$

Diagonal elements are given by

$$
\begin{aligned}
A_{mm} &= \tfrac{k_0\eta_0 w_m}{4}\left\{1 + i\tfrac{2}{\pi}\left[ln\left(\tfrac{\gamma k_0 w_m}{4}\right)\right]\right\} \\
C_{mm} &= \tfrac{k_d\eta_d w_m}{4}\left\{1 + i\tfrac{2}{\pi}\left[ln\left(\tfrac{\gamma k_d w_m}{4}\right)\right]\right\} \\
B_{mm} &= -\tfrac{1}{2} \\
D_{mm} &= \tfrac{1}{2}
\end{aligned}
\tag{3.36}
$$

To proceed with the derivation of the T-matrix, we need to derive expressions for the J and K vectors in terms of block matrices A, B, C and D. This can be done by employing a blockwise matrix inverse formula,

$$
\begin{bmatrix} A & B \\ C & D \end{bmatrix}^{-1} = \begin{bmatrix} \bar{A} & \bar{B} \\ \bar{C} & \bar{D} \end{bmatrix}, \tag{3.37}
$$

$\bar{A}$, $\bar{B}$, $\bar{C}$, $\bar{D}$ are given by:

$$\begin{aligned}
\bar{A} &= (A - BD^{-1}C)^{-1} \\
\bar{B} &= -(A - BD^{-1}C)^{-1}BD^{-1} \\
\bar{C} &= -D^{-1}C(A - BD^{-1}C)^{-1} \\
\bar{D} &= D^{-1} + D^{-1}C(A - BD^{-1}C)^{-1}BD^{-1}
\end{aligned} \tag{3.38}$$

Vectors J and K can be expressed as $J = \bar{A}E^{inc}$ and $K = \bar{C}E^{inc}$. The expression for the scattered electric field (Equation 3.31) has two components that look very similar to the scattered electric and magnetic fields for the PEC cases. Following similar steps, a T-matrix for a dielectric cylinder for TM polarization can be shown to be:

$$T = -\frac{k_0\eta_0 w_m}{4}P^{\dagger}\bar{A}P + \frac{k_0 w_m}{8}(P^{+} + P^{-})\bar{C}P \tag{3.39}$$

3.2.4 TE Dielectric

The scattered magnetic field in the case of a dielectric cylinder for TE polarization can be expressed as:

$$H^s = \frac{\partial A_y}{\partial x} - \frac{\partial A_x}{\partial y} - j\frac{k_0}{\eta_0}F_z \tag{3.40}$$

An expression for the T-matrix can be obtained following a similar procedure as in the TM dielectric case. Alternatively, the result can be obtained directly from the solution to the TM dielectric case by the application of duality. Using duality, the

expression for the off-diagonal entries of the impedance matrix become:

$$\begin{aligned} A_{mn} &= \tfrac{k_0 w_m}{\eta_0 4} H_0^1(k_0 R_{mn}) \\ C_{mn} &= \tfrac{k_d w_m}{\eta_d 4} H_0^1(k_d R_{mn}) \end{aligned}$$

$$\begin{aligned} B_{mn} = \tfrac{ik_0 w_m}{4} (\sin\Omega_n \tfrac{x_m - x_n}{R_{mn}} - \\ \cos\Omega_n \tfrac{y_m - y_n}{R_{mn}}) H_1^1(k_0 R_{mn}) \end{aligned} \tag{3.41}$$

$$\begin{aligned} D_{mn} = \tfrac{ik_d w_m}{4} (\sin\Omega_n \tfrac{x_m - x_n}{R_{mn}} - \\ \cos\Omega_n \tfrac{y_m - y_n}{R_{mn}}) H_1^1(k_d R_{mn}) \end{aligned}$$

The expressions for the diagonal elements of the impendece matrix are:

$$\begin{aligned} A_{mm} &= \tfrac{k_0 w_m}{\eta_0 4} \left\{ 1 + i\tfrac{2}{\pi} \left[ln\left(\tfrac{\gamma k_0 w_m}{4}\right)\right] \right\} \\ C_{mm} &= \tfrac{k_d w_m}{\eta_d 4} \left\{ 1 + i\tfrac{2}{\pi} \left[ln\left(\tfrac{\gamma k_d w_m}{4}\right)\right] \right\} \\ B_{mm} &= -\tfrac{1}{2} \\ D_{mm} &= \tfrac{1}{2} \end{aligned} \tag{3.42}$$

Vectors J and K can be expressed as $J = \bar{C} H^{inc}$ and $K = \bar{A} H^{inc}$. The T-matrix for the dielectric cylinder for TE polarization becomes:

$$T = -\frac{k_0 w_m}{\eta_0 4} P^{\dagger} \bar{A} P - \frac{k_0 w_m}{8} (P^{+} + P^{-}) \bar{C} P \tag{3.43}$$

3.3 Validation and Sensitivity to the shape of the cylinder

To check the validity of the derived expressions, Radar Cross sections are compared with the values given by analytical expressions in [25] for the infinite circular cylinder. A large number of discretization segments and harmonics is used to test the agreement

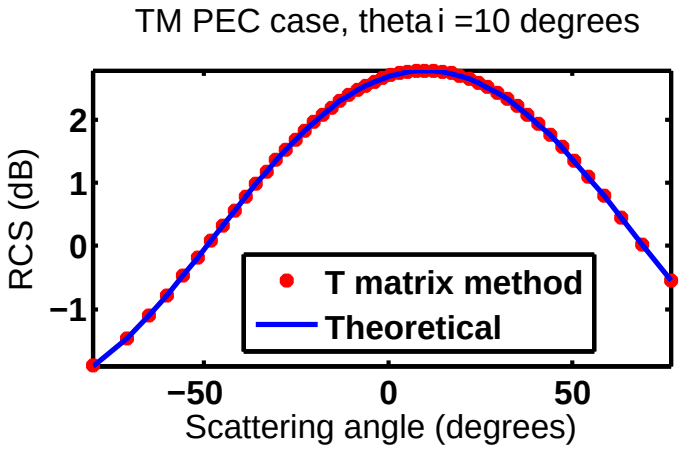

Figure 3.1: Comparison between analytical and T-matrix method for the TM-PEC case. Parameters: f = 300 MHz, Number of segments: M=161, radius of the cylinder: $r = \frac{1}{2\pi}$

between the two methods. Figure 3.1 compares the analytical and T-matrix method results for a metallic cylinder and TM polarization. The validation graphs were produced for the incidence angle of 10°. Since contributions of the discrete segments for the TM-PEC case are independent of the segment orientation, this case produces the best agreement with theoretical results even for relatively coarse discretization. Figure 3.2 shows the comparison between analytical expressions for circular cylidner and T-matrix method for the TE-PEC case. As can be observed from the figure, when sufficiently fine discretization is used, the graphs show excellent agreement. However, unlike the TM-PEC case, much finer discretization is necessary to achive the same level of agreement. Figure 3.3 shows the comparison for the TM dielectric case. The relative dielectric constant was 2 for this case. There is excellent agreement between the analytical results for circular cylinder and the results obtained from the T-matrix method. Figure 3.4 depicts excellent agreement for the TE dielctric case. Generally, the magnitude for the cross section is greater for TM cases.

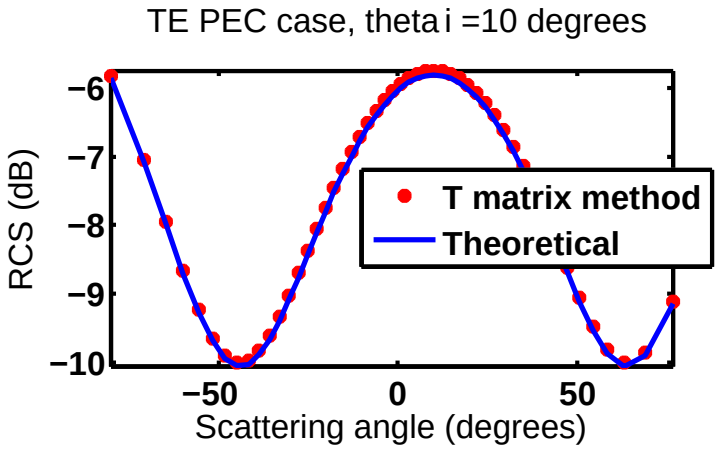

Figure 3.2: Comparison between analytical and T-matrix method for the TE-PEC case. Parameters: f = 300 MHz, Number of segments: M=161, radius of the cylinder: $r = \frac{1}{2\pi}$

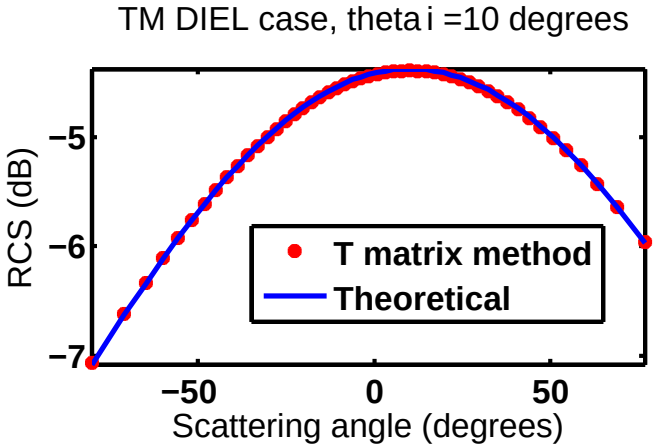

Figure 3.3: Comparison between analytical and T-matrix method for the TM-Dielectric case. Parameters: f = 300 MHz, Number of segments: M=161, radius of the cylinder: $r = \frac{1}{2\pi}$, $\epsilon_d = 2$

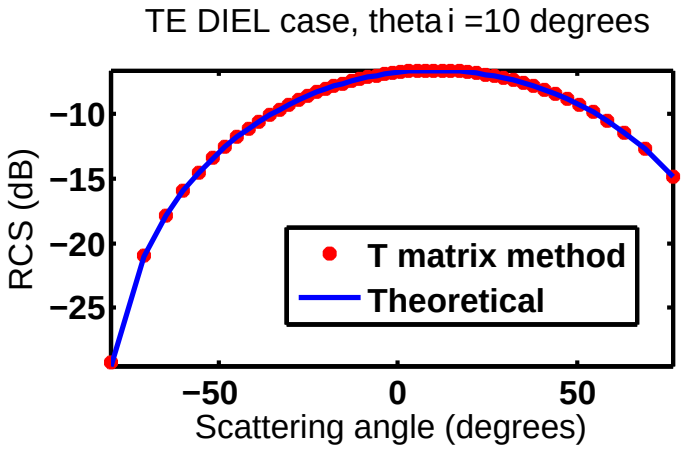

Figure 3.4: Comparison between analytical and T-matrix method for TE-Dielectric case. Parameters: f = 300 MHz, Number of segments: M=161, radius of the cylinder: $r = \frac{1}{2\pi}$, $\epsilon_d = 2$

3.3.1 Accuracy vs the Number of Segments

Generally, the computational complexity of a standard MOM algorithm is $O(n^3)$, where n is the number of segments. Using conjugate gradient and fast miltipole methods the computational comlexity of the algorithm can be reduced to $O(n^2)$ and $O(n \log n)$ respectively. Nonetheless, it is imperative to reduce the number of segments as much as the accuracy requirements allow. As evidenced by figure 3.5, fewer than 20 segments per wavelength are necessary to be within 1% of the analytical solutions for the TM-PEC case. Since only the coordinates of the centers of the segments affect the solution, coarse discretization introduces little error. For the TE-PEC case (see figure 3.6) orientation of every segment determines the contribution to the total electric field and therefore coarse discretization generates significantly higher error than the TM-PEC case. Nearly 5 times as many segments are necessary to reach the same level of accuracy as in the TM-PEC case.

3.3.2 Size of a T Matrix

Theoretically, there is an infinite number of harmonics contributing to the scattered field. To make T-matrix equations computationally practical, the infinite sum-

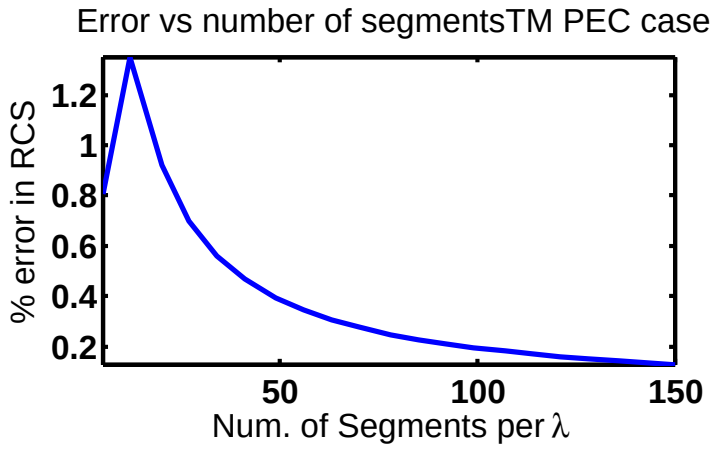

Figure 3.5: Percent error vs. the number of segments per wavelength for the TM-PEC case. Parameters: f = 300 MHz, radius of the cylinder: $r = \frac{1}{2\pi}$

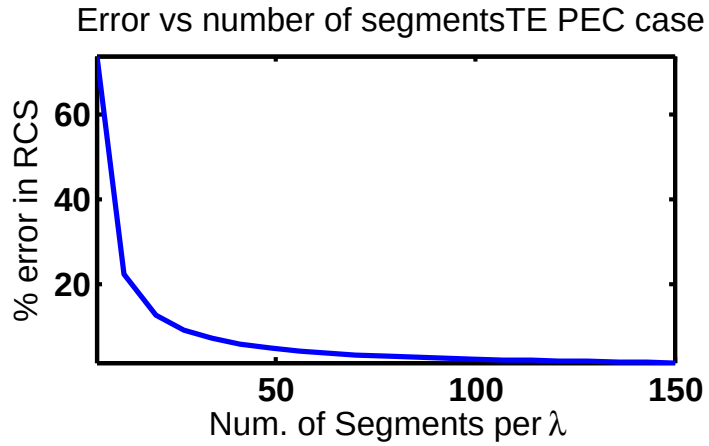

Figure 3.6: Percent error vs. the number of segments per wavelength for the TE-PEC case. Parameters: f = 300 MHz, radius of the cylinder: $r = \frac{1}{2\pi}$

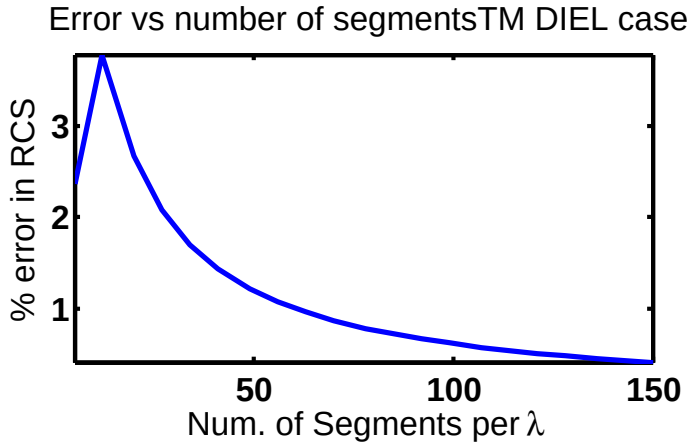

Figure 3.7: Percent error vs. the number of segments per wavelength for TM-Dielectric case. Parameters: f = 300 MHz, radius of the cylinder: $r = \frac{1}{2\pi}$, $\epsilon_d = 2$

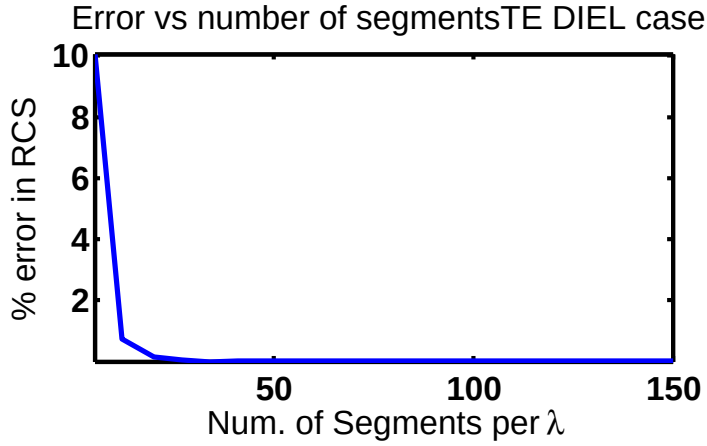

Figure 3.8: Percent error vs. the number of segments per wavelength for TE-Dielectric case. Parameters: f = 300 MHz, radius of the cylinder: $r = \frac{1}{2\pi}$, $\epsilon_d = 2$

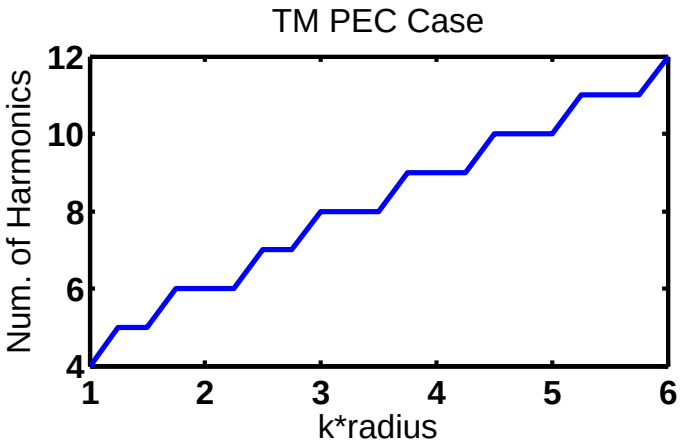

Figure 3.9: Number of harmonics N vs. the electrical size of an object for the TM-PEC case. Note, there is an equal number of negative harmonics making the total number of terms in the series $2N + 1$

mations are truncated at some number N making the size of the T matrix $2N + 1$ by $2N + 1$. There is a need for a method to determine how many harmonics are necessary to be incorporated into the T matrix to adequately represent the field scattered by an object. The method used in this work relies on the condition number of the T matrix. Generally, the largest contributions come from the first few harmonics. Eventually, the contributions from the harmonics become very small compared to the largest contribution, resulting in ill-conditioning of the T-matrix. The rate of convergence of the series depends on the electric size of the cylinder (size normalized by the wavelength). For small cylinders the series converges very rapidly and only a few harmonics are necessary to adequately represent the target. Figures 3.9– 3.12 show the truncation number vs the radius scaled by the wavenumber that would produce a condition number of 10000. The condition number is chosen rather arbitrarily but it provides a clue to the dependence of the number of harmonics vs. the size of the object for four difference cases.

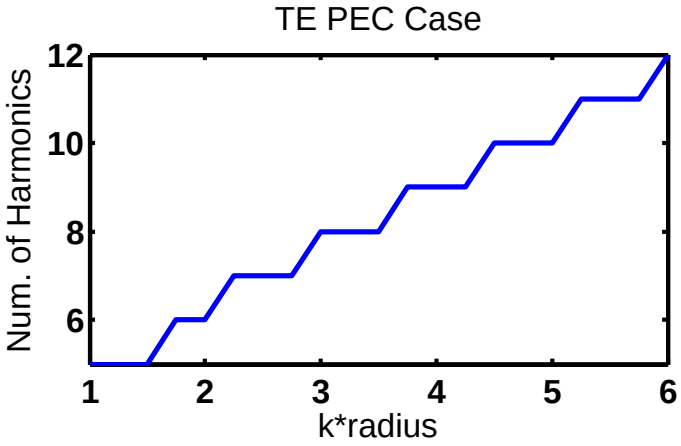

Figure 3.10: Number of harmonics N vs. the electrical size of an object for the TE-PEC case. Note, there is an equal number of negative harmonics making the total number of terms in the series $2N + 1$

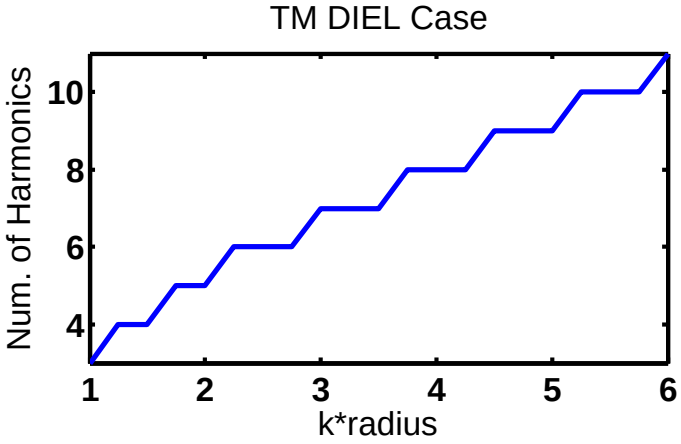

Figure 3.11: Number of harmonics N vs. the electrical size of an object for the TM-Dielectric case. Note, there is an equal number of negative harmonics making the total number of terms in the series $2N + 1$. In this case, $\epsilon_d = 2$

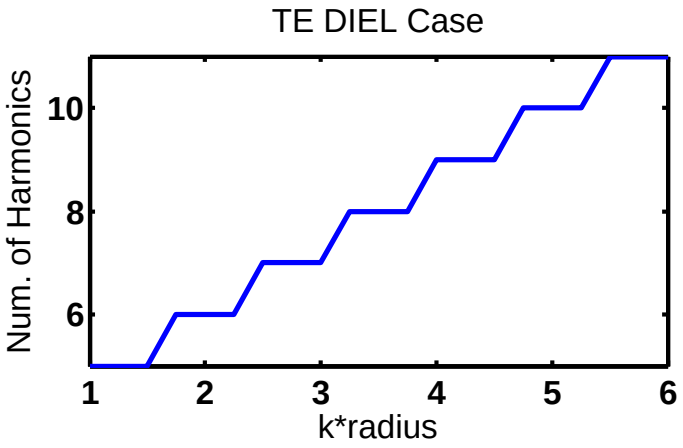

Figure 3.12: Number of harmonics N vs. the electrical size of an object for the TE-Dielectric case. Note, there is an equal number of negative harmonics making the total number of terms in the series $2N + 1$. In this case, $\epsilon_d = 2$

3.3.3 Sensitivity to the Shape of an Object

Many previous works in through-the-wall and subsurface imaging have approximated non-circular objects as circular cylinders. In this work, scattering from a smooth non-circular object is compared to a circular cylinder of the same perimeter. The goal of the study is to examine the sensitivity of cross section to object shape for all four cases, as well as to estimate the error of modeling a non-circular object as a circular cylinder. Figure 3.13 depicts a non-circular shape constructed by inserting a rectangle in the middle of a circle. The parameters of the object are the radius of the circle and the length of the rectangle (the width being equal to the diameter of the circle). Figures $3.13 -$ 3.17 compare RCS plots for four cases. Since for the TM-PEC case the orientation of the segments does not affect the imepedance matrix, approximating a smooth non-circular cylinder with a circular cylinder produces very little error. Obviously the low sensitivity to shape could be a significant challenge to classification of objects in through-the-wall or other imaging applications. The TE-PEC case, on the other hand, displays the greatest sensitivity to shape.

To further explore the sensitivity to the shape of a non-circular cylinder the cylin-

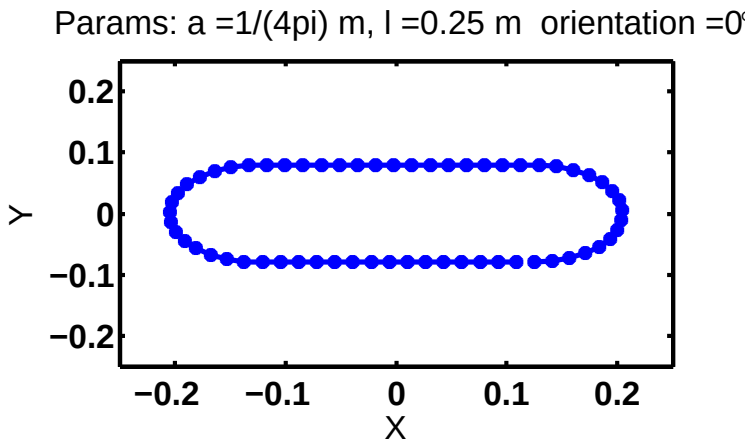

Figure 3.13: Non-circular cylinder at 0°. Non-circular cylinder is constructed by inserting a rectangle in the middle of a circle

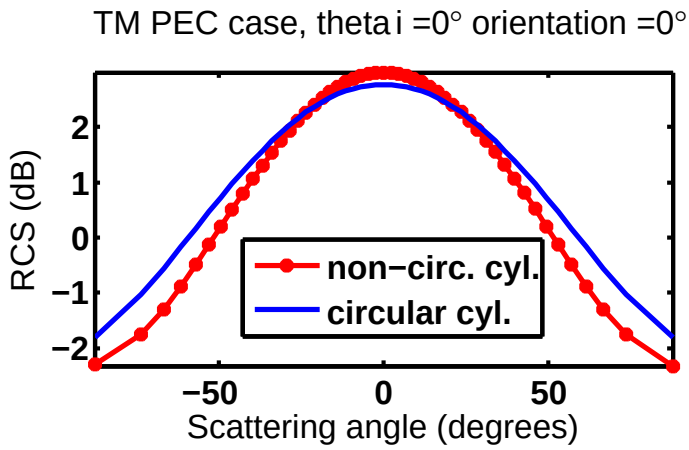

Figure 3.14: Scattering from non-circular and circular cylinders for the TM-PEC case

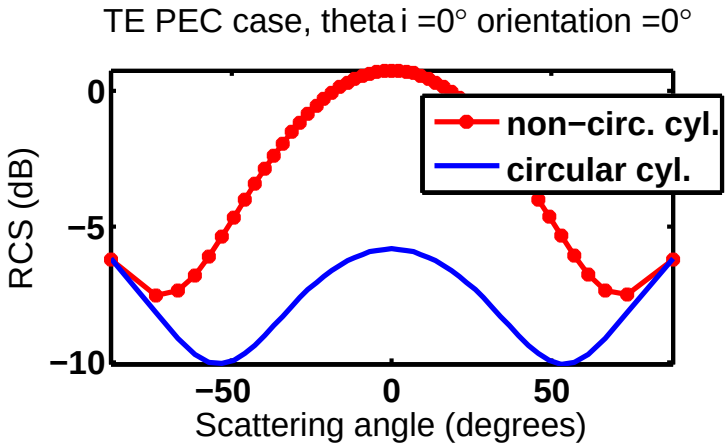

Figure 3.15: Scattering from non-circular and circular cylinders for the TE-PEC case

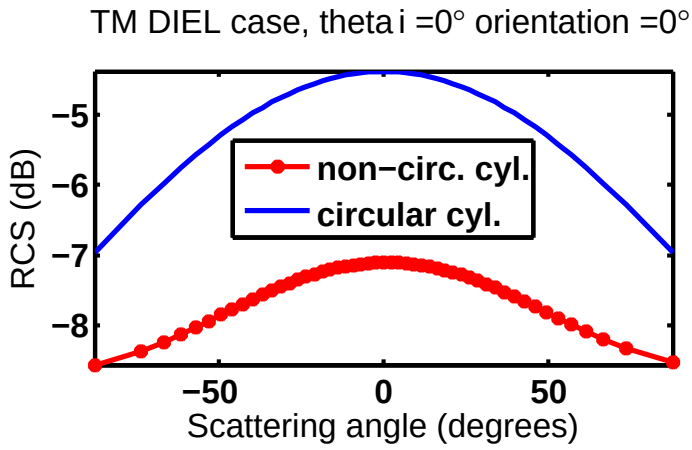

Figure 3.16: Scattering from non-circular and circular cylinders for the TM-Dielectric case ($\epsilon_d = 2$)

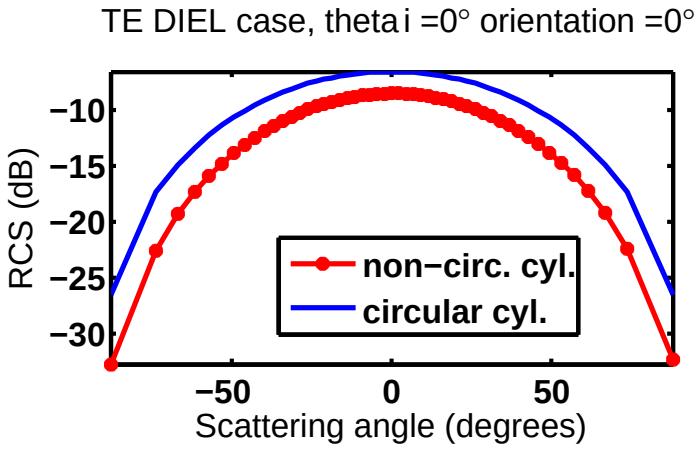

Figure 3.17: Scattering from non-circular and circular cylinders for the TE-Dielectric case ($\epsilon_d = 2$)

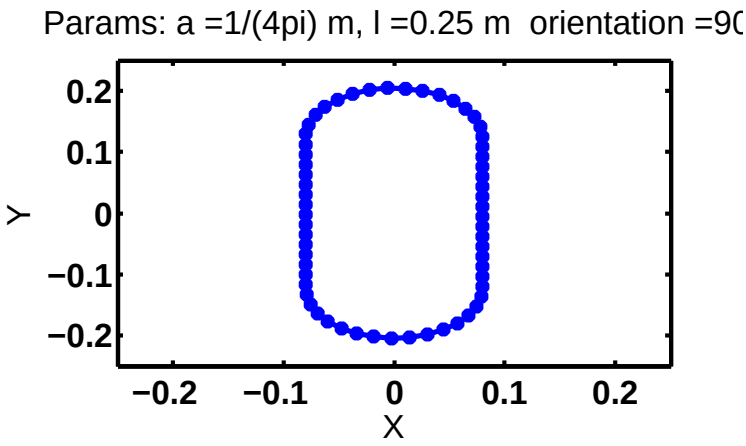

Figure 3.18: Non-circular cylinder at 90°. Non-circular cylinder is constructed by inserting a rectangle in the middle of a circle and rotating the result by 90°

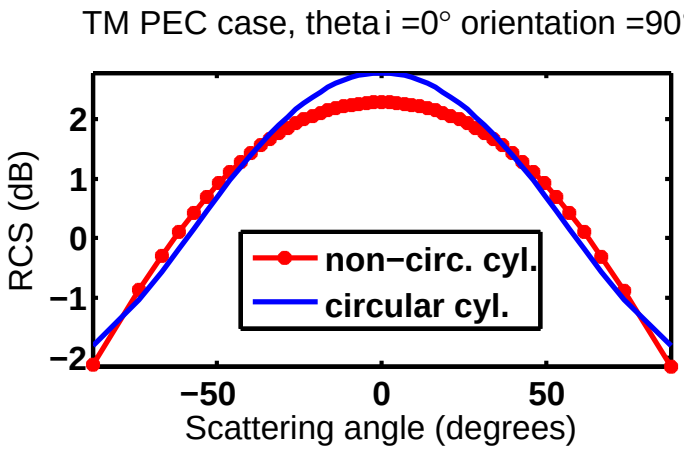

Figure 3.19: Scattering from non-circular cylinder (rotated by 90°) for the TM-PEC case

der in the previous example is rotated by 90° as depicted in figure 3.18. As in the previous example, the TE-PEC case displays the greatest and TM PEC the least sensitivity to shape.

3.4 R matrix of a cylinder

In order to compute the scattering coefficient for a cylinder-wall combination, a reflection matrix for a single cylinder needs to be computed. Reflection and transmis-

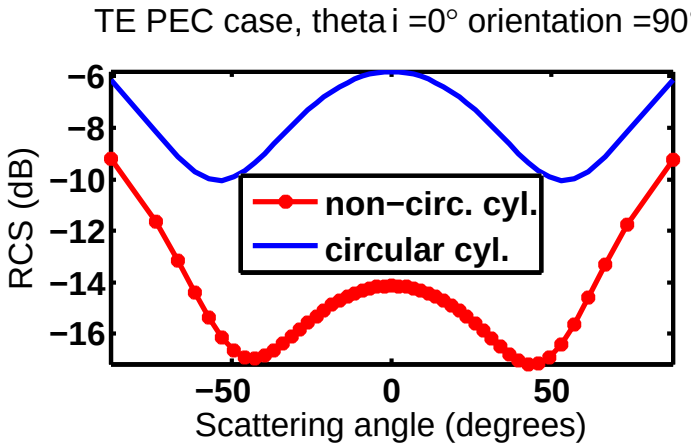

Figure 3.20: Scattering from non-circular cylinder (rotated by 90°) for the TE-PEC case

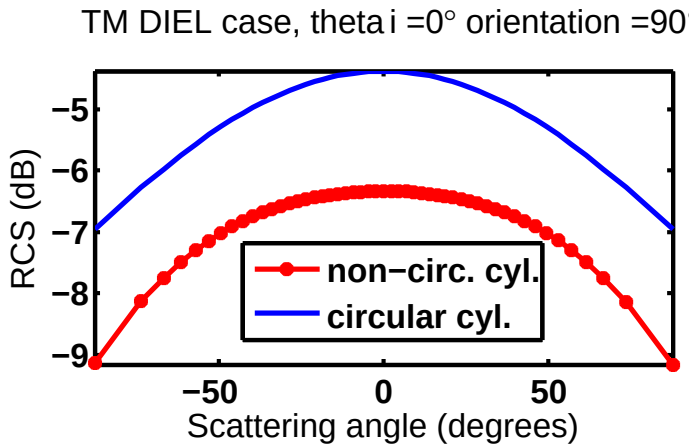

Figure 3.21: Scattering from non-circular cylinder (rotated by 90°) for the TM-Dielectric case ($\epsilon_d = 2$)

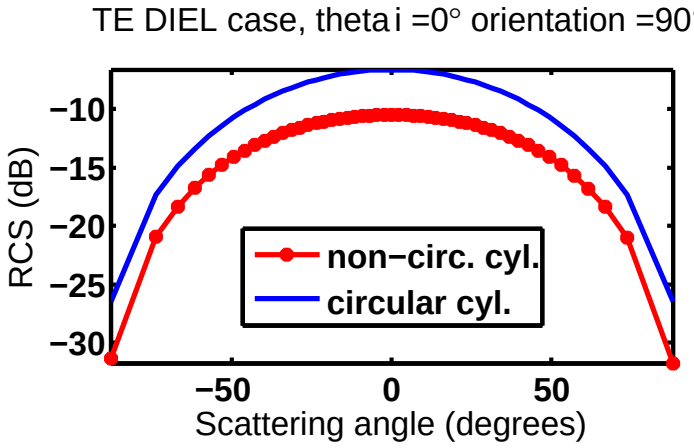

Figure 3.22: Scattering from non-circular cylinder (rotated by 90°) for the TE-Dielectric case ($\epsilon_d = 2$)

sion matrices for a periodic array of circular cylinders have been derived in [26]-[27]. When the spacing between the cylinders is large, the interaction between the cylinders can be neglected, producing an approximate solution for the scattering from a single cylinder. In order to ensure proper mode matching, the period of the cylinders has to be identical to the period used in the computation of the reflection and transmission matrices for the non-smooth interfaces. The reflection matrix for a periodic array of cylinders is given by

$$[R_{cyl}] = [U]([I] - [T][XC])^{-1}[T][P] \tag{3.44}$$

where $[XC]$ is a matrix that accounts for the cross coupling between the cylinders. When the poriod between the cylinders is large, $[XC]$ vanishes transforming equation 3.44 to

$$[R_{cyl}] = [U][T][P] \tag{3.45}$$

Matrices $[U]$ and $[P]$ are given by

$$U_{nm} = \frac{2(-i)^m}{kL\cos\theta_n} e^{im(\theta_n - \frac{\pi}{2})} \tag{3.46}$$

$$P_{mn} = i^m e^{im(\theta_n - \frac{\pi}{2})} \tag{3.47}$$

where L is the period of the cylinders (must be the same for all interfaces for mode matching), m denotes the m^{th} harmonic, n and θ_n are the n^{th} Floquet mode and angle of the n^{th} Floquet mode, respectively. Matrix P transforms the n^{th} Floquet mode into the m^{th} cylindrical harmonic; matrix U tranforms the m^{th} cylindrical harmonic into the n^{th} plane wave (Floquet mode); matrix T is a T-matrix for a single cylinder.

3.5 Scattering from a cylinder behind a non-smooth wall

Many through-the-wall, subsurface testing, and imaging applications involve objects that can be modeled as 2-D cylinders of arbitrary cross section behind a non-smooth dielectric wall. The cylinder can be either metallic or dielectric. Figure 3.23 depicts a schematic view of the target: a periodic interface is separated from the rough interface by a distance d_1 and the rough interface is separated from the center of the cylinder by distance d_2. To obtain a reflection matrix for the entire complex target, a scattering matrix technique is applied recursively to the layers from the bottom up. First, the total reflection matrix is computed for the rough interface - cylinder subsystem:

$$[R_{RC}] = [R_2] + [\tilde{T_2}][\phi_1][R_3]([I] - [\phi_2][\tilde{R_2}][\phi_2][R_3])^{-1}[\phi_2][T_2] \tag{3.48}$$

$[R_3]$ is the reflection matrix of an individual cylinder and matrices with a subscript 2 pertain to the rough interface. Now, the rough surface- cylinder subsystem can be replaced with an interface having a reflection matrix R_{RC}. The total reflection matrix for the entire system becomes

$$[R_t] = [R_1] + [\tilde{T_1}][\phi_1][R_{RC}]([I] - [\phi_1][\tilde{R_1}][\phi_1][R_{RC}])^{-1}[\phi_1][T_1] \tag{3.49}$$

Figure 3.24 depicts the sensitivity to the presence and the shape of the cylinder behind a non-smooth dielectric wall for the TM-PEC case. The results show a strong sensitivity to the presence of the cylinder. However, in the TM-PEC case the sensitivity to the shape of the cylinder is weak (about 1 dB) and probably cannot be reliably measured in practice. Simulation parameters for Figures 3.24- 3.26 are presented in Table 3.1. Figure 3.25 shows the results for TE PEC case. While the sensitivity to the presence of the cylinder is lower (but still more than enough for detection), the

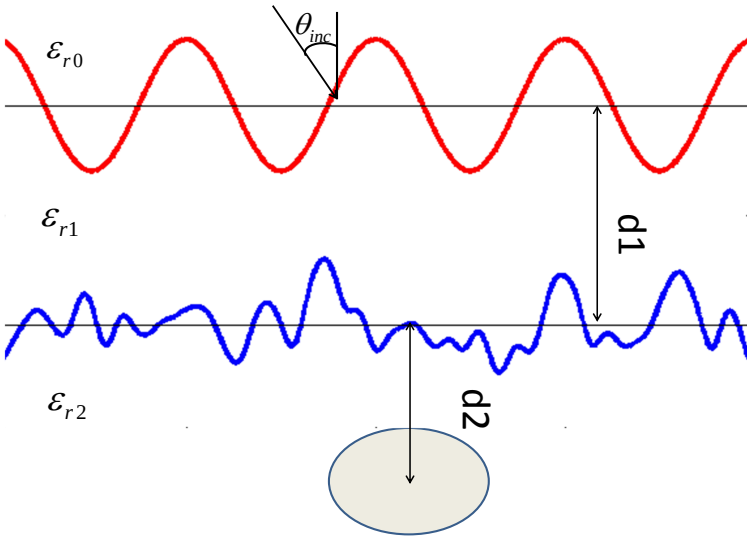

Figure 3.23: Non-circular cylinder below two non-smooth interfaces. The center of the 2D cylinder is separated from the mean height of the rough interface by a distance d_2

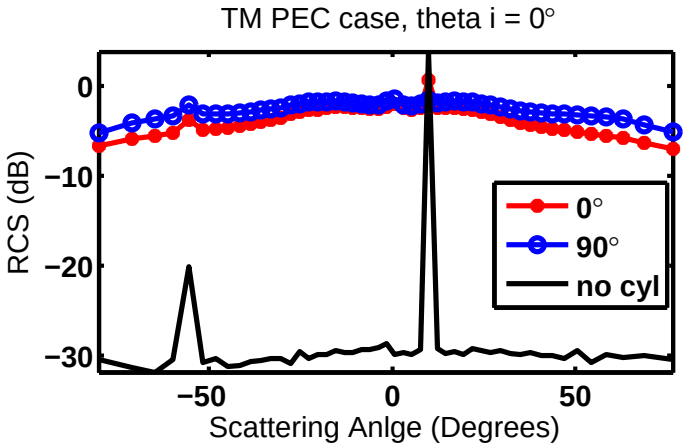

Figure 3.24: Scattering from non-circular cylinder behind non-smooth dielectric wall for the TM-PEC case. The cylinder used is depicted on Figure 3.13. While the cylinder is clearly detectable (as evidenced by large difference in observed RCS) the TM-PEC case displays only a weak sensitivity to the orientation of the cylinder.

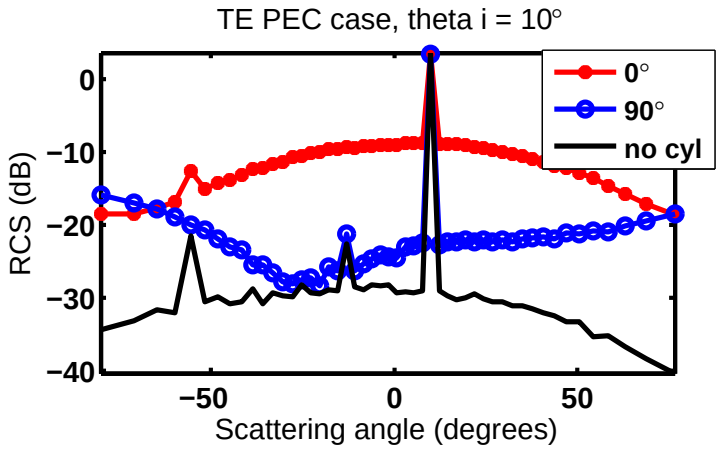

Figure 3.25: Scattering from non-circular cylinder behind non-smooth dielectric wall for the TE-PEC case. The cylinder used is depicted on Figure 3.13. The observed cross section is strongly dependent on the orientation of the cylinder

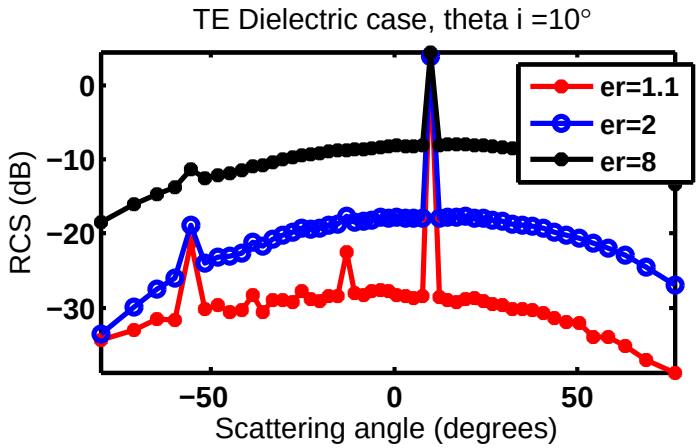

Figure 3.26: Scattering from non-circular cylinder behind non-smooth dielectric wall for the TE-Dielectric case. The cylinder used is depicted on Figure 3.13. The curves show the sensitivity of the RCS to the dielectric constant of the cylinder

	Figure 3.24	Figure 3.25	Figure 3.26
Number of Floquet modes	61	61	61
Number of pts. for each interface	1024	1024	1024
Number of realizations	85	85	85
Frequency	300 MHz	300 MHz	300 MHz
Period (for mode matching)	25 m	25 m	25 m
ϵ_r of the wall	2	2	2
Wall thickness	.5 m	.5 m	.5 m
Wall to the cylinder	1m	1m	1m
Amplitude of the periodic surface	2 cm	2 cm	2 cm
Period of the periodic surface	1 m	1 m	1 m
σ_{rms} of the rough surface	2 cm	2 cm	2 cm
Correlation length	20 cm	20 cm	20 cm
Radius of the cylinder (circular part)	$\frac{1}{4\pi}$	$\frac{1}{4\pi}$	$\frac{1}{4\pi}$
Length param. of the cylinder	25 cm	25 cm	25 cm
Number of discretization segments	161	161	161
Number of harmonics	35	35	35
Cylinder orientation	0, 90	0, 90	0
Cylinder ϵ_r	PEC	PEC	1.1, 2, 8
Case	TM PEC	TE PEC	TE Dielectric

Table 3.1: Non-circular cylinder behind non-smooth wall simulation parameters

simulation displays significant sensitivity to the shape of the cylinder. The sensitivity to shape is important in through-the-wall imaging and characterization of burried objects applications. Figure 3.26 explores the sensitivity of RCS to the relative dielectric constant of the cylinder for the TE Dielectric case. Based on the graph, the sensitivity to the relative dielectric constant of the cylinder makes it possible to develop inversion algorithms that would allow us to determine the dielectric properties of the cylinder and identify the material from which the cylinder was made.

3.6 Conclusion

In this chapeter a new and efficient approach for computation of T-matrices for $2D$ cylinders of arbitrary cross sections was demostrated. Once the T-matrices are computed, the resulting matrix is transformed to a reflection matrix for an individual cylinder. The reflection matrix can be easily cascaded with transmission and reflection

matrices for one or more interfaces. This approach is efficient and flexible which allows it to be applied to modeling many natural and artificial objects, from buried pipes underneath layered soil to detection of objects behind non-smooth walls.

CHAPTER IV

Retrieval of Parameters for Three-Layer Media

4.1 Introduction

A solution to the inverse problem for a three-layer medium with non-smooth boundaries, representing a large class of natural subsurface structures, is developed in this chapter using simulated radar data. The retrieval of the layered medium parameters is accomplished as a sequential nonlinear optimization process starting from the top layer and then progressively characterizing the layers below. The optimization process is achieved by an efficient iterative technique built around the solution of the forward scattering problem. To be efficiently utilized in the inverse problem, the forward scattering model is simulated over a wide range of unknowns to obtain a complete set of subspace-based equivalent closed-form models that relate the radar backscattering coefficients to the sought-for parameters, including dielectric constants of each layer and the thickness of the middle layer. The inversion algorithm is implemented as a modified conjugate-gradient-based nonlinear optimization. It is assumed that multifrequency radar measurements are available from tower-mounted or airborne platforms, at radar frequencies of L-band, P-band (UHF), and/or VHF. It is shown that this technique results in accurate retrieval of surface and subsurface parameters, even in the presence of noise.

4.2 Closed Form Representations

4.2.1 Obtaining Analytical Expressions

Even though the computational complexity of the forward model based on EBCM is significantly less than a fully numerical technique such as MOM, it is still too costly for use in most iterative inversion algorithms. This problem is especially serious for global optimization algorithms that often require hundreds of thousands of iterations to converge. Local optimization methods usually converge faster but they require multiple computations of partial derivatives which quickly accumulates significant errors if done numerically, increasing the likelihood of being trapped in a local minima. To arrive at a model that is more suitable for inversion, we use the full forward scattering model to derive an equivalent analytic (closed-form) representation by pre-computing the backscattering coefficients for a comprehensive set of parameters, followed by several function fits. A preliminary version of this equivalent-model approach was developed in [28] for scattering from vegetation canopies. More specifically, the full model is simulated for a range of parameters such as those related to the dielectric constants (water content), surface height statistics, and layer separation. Then, the dependence on each of these parameters is sequentially modeled using much simpler, analytically differentiable functions, such as polynomials of arbitrary orders. The result is a multidimensional nonlinear, but closed-form (analytic) function. Once the proper closed-form model is developed, the subsequent evaluations of the forward model are extremely fast and the forward model is suited for both local and global inversion techniques. The derivation of this analytic-form model has several intricacies, which are discussed later in this chapter.

4.2.2 Sequential Layer Characterization

The inversion process requires at least as many independent data points (measurements) as there are unknowns. The initial overhead cost of simulating the function for a range of values of all of the unknowns may be too large to be practical, especially considering that the lower interface is a random rough surface, requiring the scattering simulation of many realizations of the surface. Therefore, a sequential layer characterization algorithm is applied by using a multifrequency radar scenario. Even if the inverse problem is solved simultaneously for the unknowns of all layers, at least two frequencies are required to obtain accurate results (see [29]). Assuming the medium between the first and second interfaces is uniform but lossy, the scattering problem is first simulated at a sufficiently high frequency such that the effects of the 2^{nd} interface are negligible. With the assumption that only the top layer affects the scattering coefficients at this frequency, the number of unknowns is greatly reduced, and the retrieval of the top-layer unknowns can be efficiently accomplished. Since the top layer is a deterministic periodic surface, there is no need for computing multiple realizations of the surface to obtain statistically representative values. With the top layer characterized, the scattering contribution of the subsurface layer can be simulated at a lower frequency. The coupling between the two interfaces is still fully represented in the solutions of the forward and inverse models through the lower frequency radar data, but the retrieval of their properties has been effectively decoupled through this approach.

4.2.3 Sensitivity to errors in Ancillary Parameters

While the forward model contains many parameters, only a few, usually parameters related to dielectric constants (for example volumetric moisture content for soils) and separation of layers are the parameters of interest. For a successful inversion, all other parameters (which we will call ancillary parameters) still have to be obtained

as well. Generally there are three methods of obtaining these parameters. These parameters can be treated as unknowns, with the inversion algorithm producing values for these parameters along with the primary sought-for parameters. While this approach is often the only feasible way to obtain ancillary parameters, it has some major drawbacks. Each additional unknown significantly slows down the initial simulation. Generally, the minimum number of simulations required to obtain a unique solution is given by:

$$N_{sim} = M \prod_{m=1}^{M} P_m \tag{4.1}$$

N_{sim} = Number of simulations,

M = Number of unknown parameters,

P_m = Number of values of the m^{th} parameter to cover the desired range.

Increasing the number of unknowns quickly leads to prohibitively costly initial simulations, as well as to the increased likelihood of the inversion algorithm converging to a local minimum. Another method for obtaining ancillary parameters is apriori approximation, provided the expected error is small and quantifiable. However, careful sensitivity analysis must precede the approximation. This method is generally only feasible if the sensitivity of the scattering coefficients to that parameter is low in the region of approximation.

Direct measurement is another alternative for obtaining ancillary parameters. Since the cost of the measurement is usually dependent on the accuracy of the measurement performed, careful sensitivity analysis is needed to estimate the maximum allowable error in the ancillary parameter that would meet the accuracy requirements for the scattering measurements. For a periodic surface the amplitude is usually an ancillary parameter, whereas the dielectric constant is a parameter of interest. Figure 4.1 shows the sensitivity of the model to errors in the amplitude. The backscattering coefficients are very sensitive to errors in the amplitude and therefore this parameter has to be obtained to a high degree of accuracy. For the rough interface, the ancillary

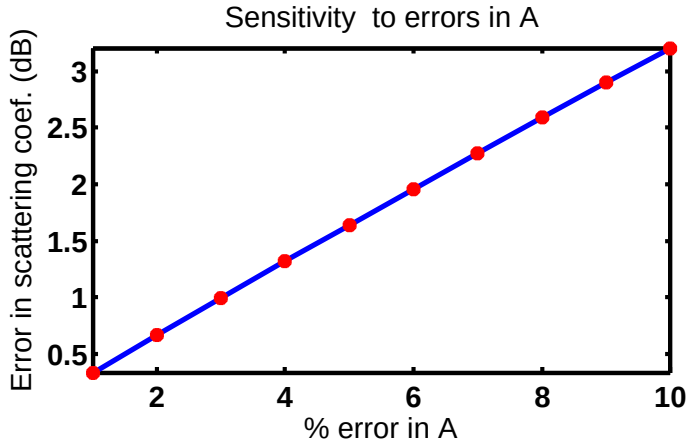

Figure 4.1: Sensitivity of errors in scattering coefficients to errors in amplitude of the periodic surface A. Error in backscattering coefficients (dB) increases almost linearly with increase in error in the surface amplitude, hence large sensitivity.

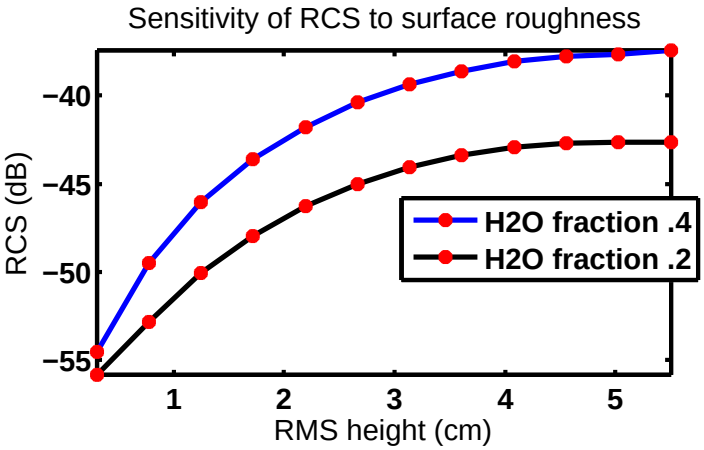

Figure 4.2: Sensitivity to errors in σ_{rms}. Sensitivity of RCS to σ_{rms} is highly variable for different ranges of σ_{rms}. The simulation was performed at $435MHz$. Simulation parameters: $A = 3cm$, $period = 1m$, correlation length $= 20cm$, layer separation $= 2m$, $\epsilon_{r1} = 5.5 + .3i$. Water fractions of .2 and .4 correspond to $\epsilon_{r2} = 11.5565 + 4.5961i$ and $\epsilon_{r2} = 26.3868 + 8.1573i$ respectively (see [30])

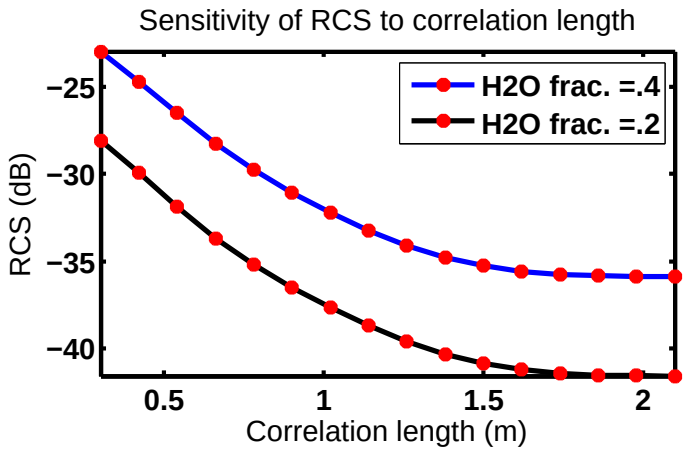

Figure 4.3: Sensitivity of RCS to correlation Length l. The sensitivity decreases significantly for larger values of l. The simulation was performed at $435MHz$. Simulation parameters: $A = 3cm$, $period = 1m$, $\sigma_{rms} = 4cm$, layer separation $= .5m$, $\epsilon_{r1} = 5.5 + .3i$.

parameters are usually surface roughness σ_{rms} and correlation length l. As can be seen from Figure 4.2, the backscattering coefficients are quite sensitive to the errors in the σ_{rms} of the lower surface. However, this sensitivity is not uniform and decreases for increased roughness. The sensitivity to errors in correlation length is relatively small and is not uniform as well (see Figure 4.3). For regions where the sensitivity is the smallest, a simple apriori approximation is enough to obtain acceptable retrieval results for other parameters of interest.

4.3 Inversion Algorithm

4.3.1 Inversion Algorithm Overview

Once the numerical simulations over the desired range of parameters are complete, special care is needed to select the proper polynomial representation for the data. While it may be tempting to fit a high-order polynomial such that the residual error is exactly zero, the polynomial function may oscillate rapidly between the sample points, which represents nonphysical behavior and significantly degrades the inversion algorithm. A lower-degree fit, on the other hand, could produce a less accu-

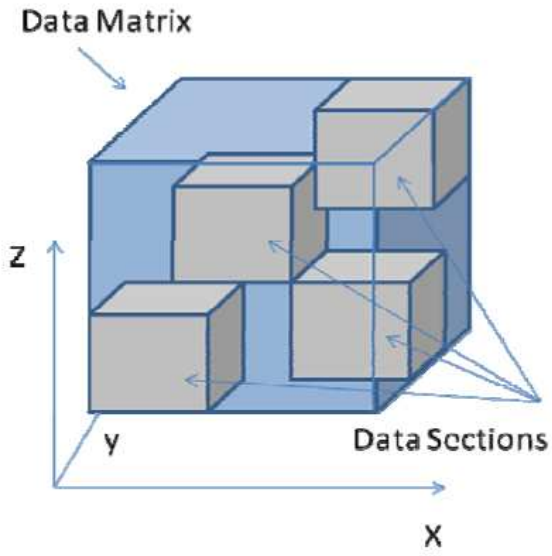

Figure 4.4: Data subspaces for the 3-D case). The total data space is broken up into smaller subspaces. The inversion algorithm is then applied to every individual subspace and the best solution is then selected.

rate function representation with errors accumulating rapidly with each subsequent dimension. To address both of these problems, the method developed here optimally balances the quality of the closed form models and the robustness of the inversion algorithm, as described below. The initial simulated data space is broken up into subspaces of the same dimension but with only a subset of the total points along each dimension (typically 4 points). For example, for the case of 3 unknown variables, the complete data space is a cube, and the subspaces are smaller cubes that completely fill the larger space. Typically, we use polynomials of 3rd order to fit the data in each subspace, resulting in an analytical model for that subspace (Figure 4.4). The 3rd order polynomials are fitted with high accuracy and generally produce non-zero 2nd order partial derivatives, which are used in a conjugate-gradient based inversion algorithm. If a unique solution for the problem exists, it must be contained in one of the data subspaces shown in Figure 4.4. The retrieval problem is solved for each individual data subspace and the best solution is then selected based on the magnitude of an appropriately defined cost function.The inversion algorithm used in this work

is a local optimizer based on the conjugate gradient method. The cost function to be minimized can be expressed as:

$$L(\mathbf{x}) = \sum_{n=1}^{N} (f_n(x_1, x_2, x_3) - f_{obs_n})^2 \tag{4.2}$$

where $\mathbf{x} = [x_1, \ldots, x_m]$ is a solution vector, with m corresponding to the dimension of the inversion, f_{obs_n} is the n^{th} component of the independent observation vector and $f_n(\mathbf{x})$ is the n^{th} estimate. The procedure starts by computing two initial vectors: $\mathbf{g_0} = \nabla L(x_0)$, and $\mathbf{d_0} = -\mathbf{g_0}$. Then, the following equation is evaluated iteratively until sufficient level of convergence or the maximum number of iterations is reached:

$$\mathbf{x_{k+1}} = \mathbf{x_k} + \lambda_k \mathbf{d_k} \tag{4.3}$$

where $\mathbf{d_{k+1}}$ and λ_k are given by:

$$\mathbf{d_{k+1}} = -\mathbf{g_{k+1}} + b_k \mathbf{d_k},\ \lambda_k = -\frac{\nabla L(x_k) \cdot \mathbf{d_k}}{\nabla(\nabla L(x_k) \cdot \mathbf{d_k}) \cdot \mathbf{d_k}} \tag{4.4}$$

$$b_k = \frac{\mathbf{g_{k+1}}^t \cdot (\mathbf{g_{k+1}} - \mathbf{g_k})}{\mathbf{g_k}^t \cdot \mathbf{g_k}} \tag{4.5}$$

Since all of the operations are performed on closed-form functions, these operations, including multiple gradient computations, are analytic and do not accumulate errors. The algorithm is very efficient compared to most global optimization techniques and usually converges in less than 50 iterations. Since the inversion algorithm is a local optimizer the convergence to the global minimum is not guaranteed [29]. Breaking up the problem into subspaces increases the chances of finding a global minimum, since the algorithm can only get trapped in the local minimum and not converge to a global minimum if both are present within one data subspace; the probability of this event is very small compared to the case where the search is over the entire data

domain.

4.3.2 Computational Efficiency of Inversion Algorithm

The inversion algorithm described in this work is an efficient local optimizer which is able to achieve high levels of accuracy in relatively few steps. As the data space is broken into subspaces, the problem is solved individually in every subspace. If a unique solution is to be obtained, and if the maximum allowable error is set to a sufficiently low value, the algorithm should only converge in one of the data subspaces and run out of the maximum allowable iterations in others. Since the majority of time is spent looking for the solution in subspaces that do not contain the global minimum, the maximum allowable number of iterations is a critical parameter for computational efficiency of the algorithm. The overall computational time beyond the initial overhead of obtaining the closed form solutions is approximately equal to:

$$t_{total} = t_{cg} \cdot N_{max} \cdot N_{subspaces} \tag{4.6}$$

t_{total} = total run time to complete the inversion process,
t_{cg} = runtime for a single iteration of CG within a subspace,
N_{max} = maximum number of iterations,
N_s = number of subspaces.
The number of iterations it usually takes to reach convergence depends on the type of closed-form function used to fit the data, the maximum allowable error, and the overall dimension of the problem. Table 4.1 summarizes the empirically found results: higher dimensions require significantly more iterations to reach convergence. The maximum acceptable value for the cost function was set to 10^{-3}. The user has a choice of setting the N_{max} parameter which is critical to the computational speed of the overall inversion algorithm. If we assume there is a unique solution and there is

Table 4.1: Maximum Number of Iterations to Converge

Dimension	Type of function	Iterations to converge
1	Cubic polynomial	8
2	Cubic polynomial	17
3	Cubic polynomial	54

no subspace overlap, the solution must be contained in only one subspace. Therefore, the algorithm runs N_{max} times in all other subspaces without reaching convergence. In the case of non-unique solutions or solutions at the boundaries of subspaces fewer iterations are typically needed since the algorithm will converge faster than N_{max} in more than one subspace.

4.3.3 Effect of Observation Parameters on Inversion Results

In order for the inversion algorithm to produce a unique solution for N independent variables there needs to be at least N independent observations. However, depending on the characteristics of the forward scattering model, there are still ambiguous cases when two or more combinations of parameters produce the same value for the backscattering coefficients. To illustrate this point using a one-dimensional case, Figure 4.5 shows the dependence of the backscattering coefficient on the layer separation at two different frequencies. Since it is a one dimensional case with the only unknown being the layer separation d, one observation could potentially be enough to obtain a unique solution. If the true value of layer separation is $d = .7m$, this value corresponds to the cross section values of -33.7 dB and -36.8 dB for 120 MHz and 150 MHz respectively. If only one observation is used, the inversion algorithm converges to two solutions for each of the frequencies (marked with asterisks) and it is impossible to pick the correct solution without additional information. However, when both observations are used, the algorithm inevitably picks out the correct solution. The same principle applies to higher dimensions.

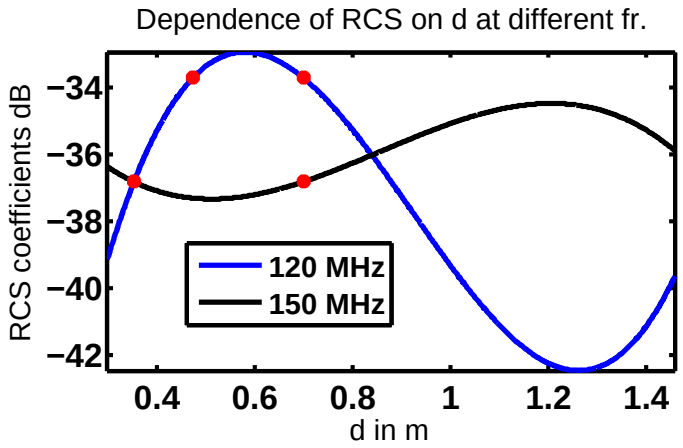

Figure 4.5: RCS vs. layer separation at two frequencies. RCS is an oscillating function of depth, especially for lossless cases, because as depth increases it periodically becomes equal to an integer multiple of half a wavelength. Therefore, more than one observation is usually necessary to obtain a unique solution.

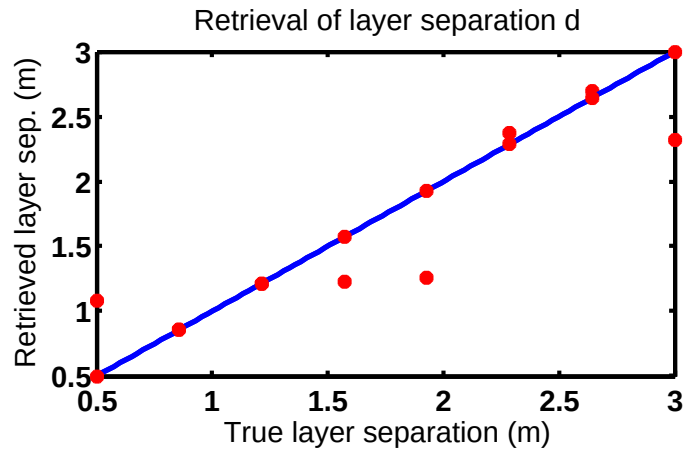

Figure 4.6: 1-D case: one observation. Only one observation is used in the inversion resulting in non-unique solutions. Parameters: $\theta_i = 40\,\text{deg}$, Amplitude $= 3cm$, $l = 20cm$, $\epsilon_{r1} = 5.5 + .3i$, $\sigma_{rms} = 7cm$, H_2O frac. $= .15$. Observation channel: $f_1 = 120MHz$

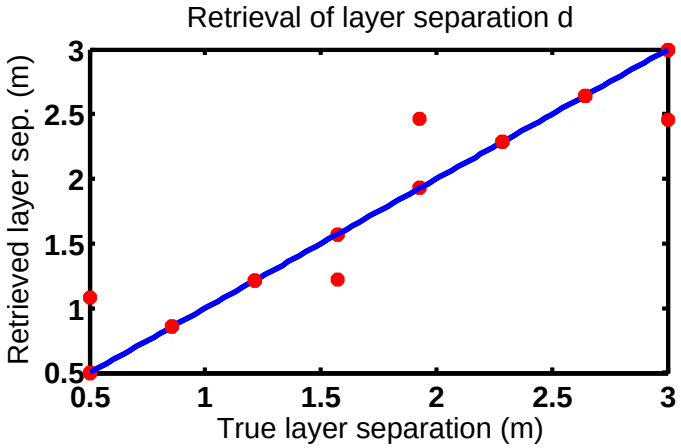

Figure 4.7: 1-D case: two closely spaced observations (in frequency). Even though two observations are used, the observations are closely spaced (in frequency) resulting in limited improvement in the quality of the inversion. Parameters: $\theta_i = 40\,\text{deg}$, Amplitude $= 3cm$, $l = 20cm$, $\epsilon_{r1} = 5.5 + .3i$, $\sigma_{rms} = 7cm$, H_2O frac. $= .15$. Observation channels: $f_1 = 120MHz$, $f_2 = 150MHz$

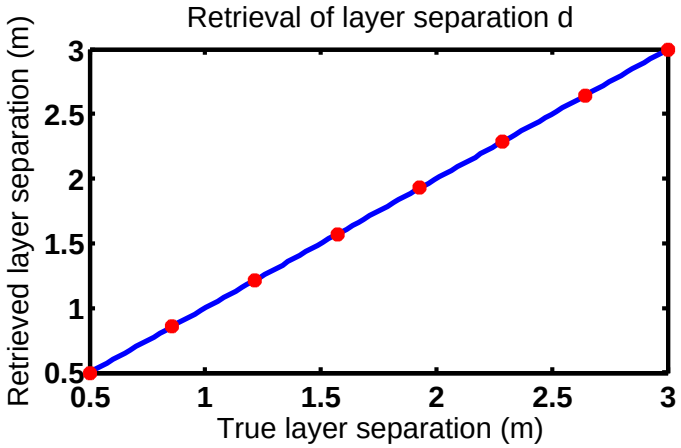

Figure 4.8: 1-D case: two separated in frequency observations. Two observations are used to produce nearly perfect results. Parameters: $\theta_i = 40\,\text{deg}$, Amplitude $= 3cm$, $l = 20cm$, $\epsilon_{r1} = 5.5 + .3i$, $\sigma_{rms} = 7cm$, H_2O frac. $= .15$. Observation channels: $f_1 = 120MHz$, $f_2 = 460MHz$

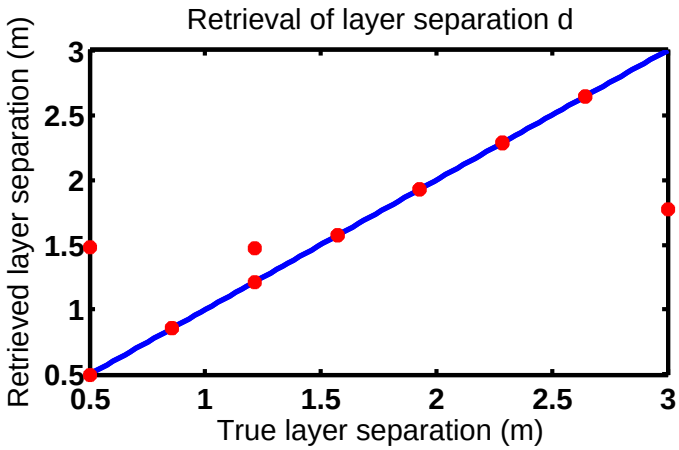

Figure 4.9: For the two dimensional case the minimum number of observations is used. The observations are closely spaced in frequency producing non-unique inversion results. Parameters: $\theta_i = 40\,\text{deg}$, Amplitude $= 3cm$, $l = 20cm$, $\epsilon_{r1} = 5.5 + .3i$, $\sigma_{rms} = 7cm$. Observation channels: $f_1 = 120MHz$, $f_2 = 150MHz$

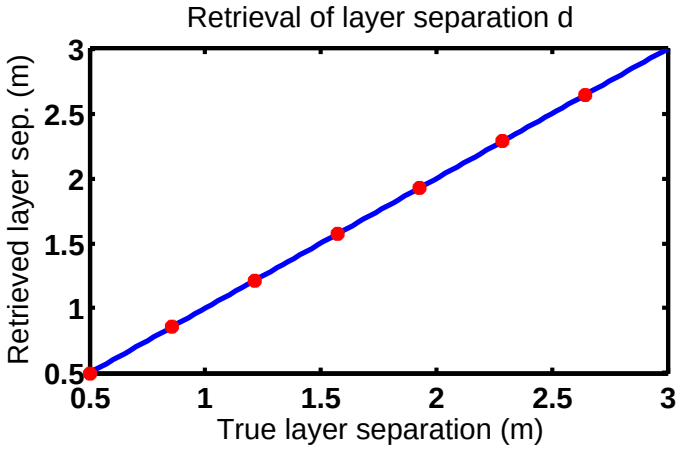

Figure 4.10: Three independent observations are used in a 2-D case resulting in significantly improved inversion results. Parameters: $\theta_i = 40\,\text{deg}$, Amplitude $= 3cm$, $l = 20cm$, $\epsilon_{r1} = 5.5 + .3i$, $\sigma_{rms} = 7cm$. Observation channels: $f_1 = 120MHz$, $f_2 = 180MHz$, $f_3 = 460MHz$

Figure 4.6 shows the results for one observation (one dimensional case). As can be seen, the algorithm often converges to multiple solutions and more observations are needed to remove the ambiguity. Introducing another observation that is closely spaced in frequency (20 MHz apart) and therefore not completely independent from the original observation helps eliminate a few double solutions but the algorithm still fails to produce a unique solution every time (see Figure 4.7) . If the second observation is replaced by one taken at a very different frequency (for example 450 MHz), the algorithm converges to a unique solution every time (see Figure 4.8). Additional observations would not result in further improvement in the absence of noise, but could be helpful in practical situations when measurement noise is present. The same trend continues for 2 and 3 dimensions (see Figures 4.9 and 4.10), although it normally takes more observations for the algorithm to converge to a correct solution every time. When applied to radar remote sensing, these observations are backscattering cross section measurements at difference frequencies, polarizations, and incidence angles. In the case of observations taken at different frequencies, the frequency separation should be large enough to ensure a necessary degree of linear independence. When observations are cross section measurements taken at frequencies that are spaced close to one another, the algorithm typically produces multiple solutions.

4.3.4 Inversion Results and Sensitivity of Errors in the Backscattering Coefficients

The algorithm described in this work is an efficient and robust method for retrieving parameters of interest from radar cross section measurements. Once the initial simulation over multiple parameters is complete and subspace-based closed-form expressions are obtained, all subsequent operations such as computing 2^{nd} order partial derivatives are analytical and therefore do not accumulate errors. The algorithm has

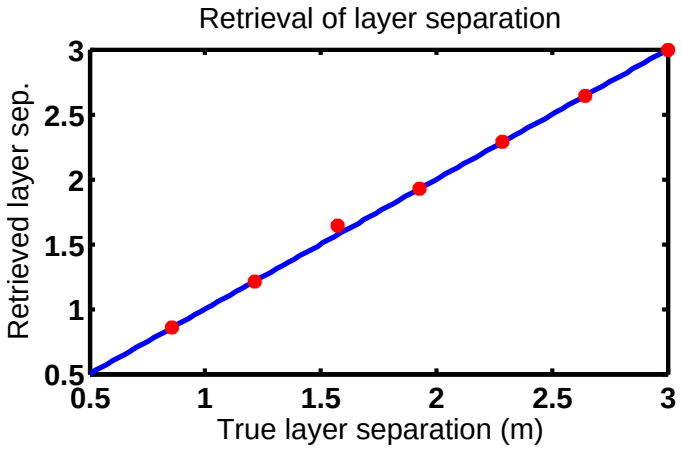

Figure 4.11: Retrieval of layer separation for 3-D errorless case. Parameters: $\theta_i = 40\,\text{deg}$, Amplitude $= 3cm$, $l = 20cm$, $\epsilon_{r1} = 5.5 + .3i$

been extensively validated, first using noise-free simulated data for a wide variety of layered-medium parameters. Figures 4.11 and 4.12 show estimated parameters vs. true values for a 3 variable inversion (the other variable being the roughness of the layer). These plots show inversion results for a three dimensional case (three unknowns) when a sufficient number of observations were included in the algorithm. In this case, six observations at different frequencies were used (120 MHz, 150 MHz, 180 MHz, 400 MHz, 435 MHz, and 460 MHz).

Since all measurements include some error, it is important to analyze the robustness of the inversion algorithm when real observations containing noise error are used. Figure 4.13 shows the same scenario as Figure 4.11 for layer separation retrieval but this time 0.1 dB of Gaussian noise was added to the observations. Increasing the error to 0.5 dB (see Figure 4.14), we can see the increase in the error in the retrieved parameters, but overall, the errors remain relatively small and the algorithm does not break down. Increasing the error to 1 dB (see Figure 4.15), we notice the further increase in error but the algorithms still performs considerably well. Similar analysis is then performed to analyze the error performace of the algorithm when retrieving the water content of the 3^{rd} layer. Typically, the sensitivity of the backscattering coefficients to the moisture content in the 3^{rd} layer is lower than to the layer separation

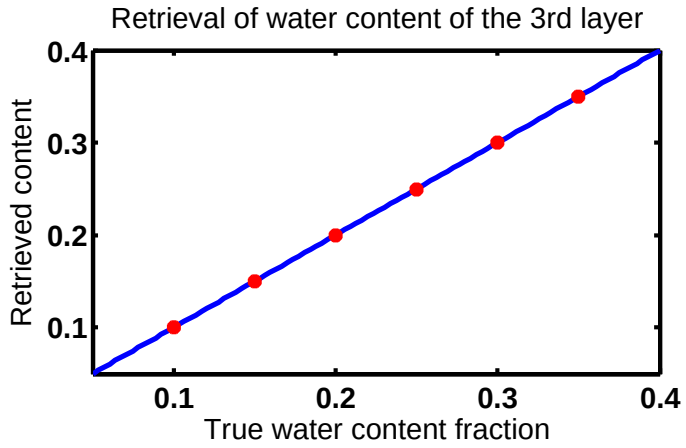

Figure 4.12: Retrieval of water content of the 3^{rd} layer for 3-D errorless case. Parameters: $\theta_i = 40\,\text{deg}$, Amplitude $= 3cm$, $l = 20cm$, $\epsilon_{r1} = 5.5 + .3i$

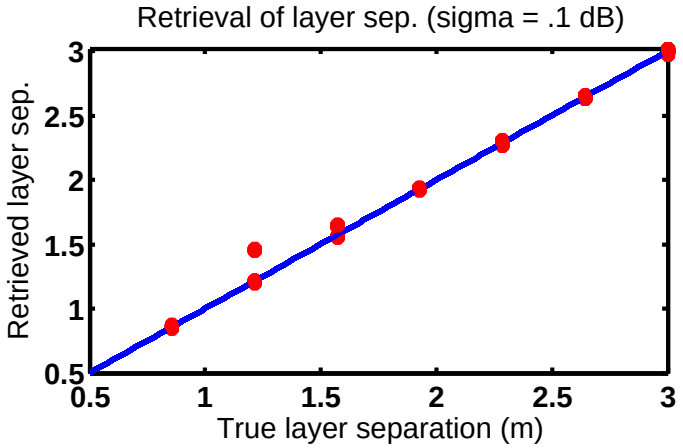

Figure 4.13: Retrieval of layer separation (3-D case). $E_{rms} = .1dB$. Parameters: $\theta_i = 40\,\text{deg}$, Amplitude $= 3cm$, $l = 20cm$, $\epsilon_{r1} = 5.5 + .3i$

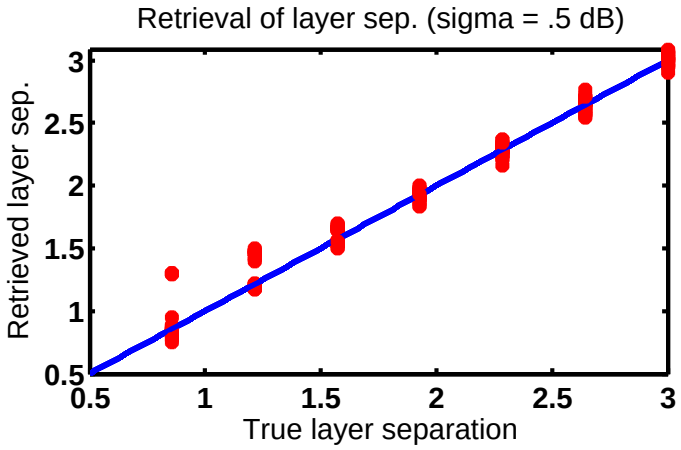

Figure 4.14: Retrieval of layer separation (3-D case). $E_{rms} = .5dB$. Parameters: $\theta_i = 40\,\text{deg}$, Amplitude $= 3cm$, $l = 20cm$, $\epsilon_{r1} = 5.5 + .3i$

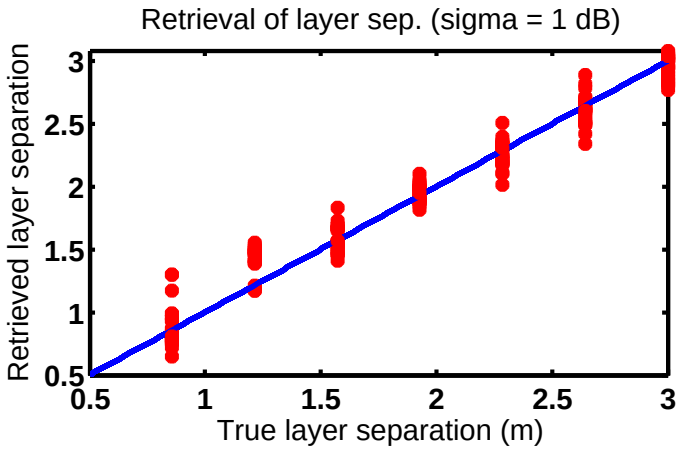

Figure 4.15: Retrieval of layer separation (3-D case). $E_{rms} = 1dB$. Parameters: $\theta_i = 40\,\text{deg}$, Amplitude $= 3cm$, $l = 20cm$, $\epsilon_{r1} = 5.5 + .3i$

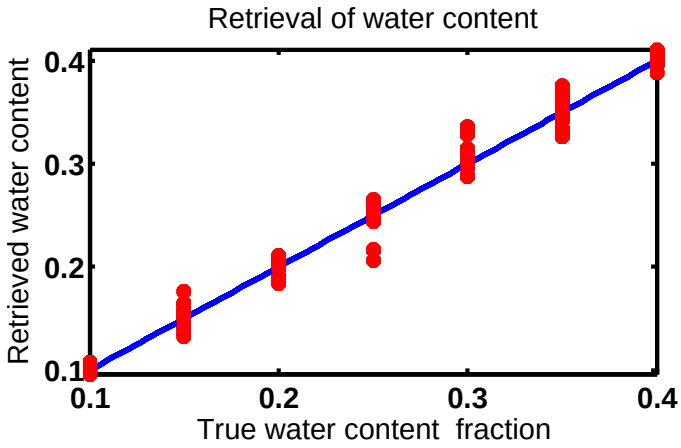

Figure 4.16: Retrieval of H_2O fraction in the 3^{rd} layer (3-D case). $E_{rms} = .1dB$. Parameters: $\theta_i = 40\,\text{deg}$, Amplitude $= 3cm$, $l = 20cm$, $\epsilon_{r1} = 5.5 + .3i$

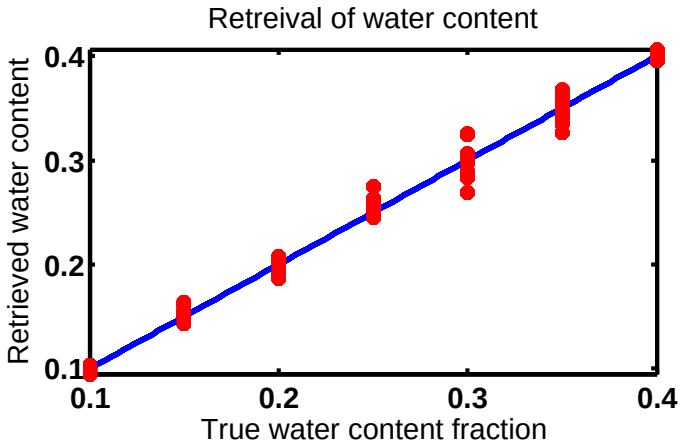

Figure 4.17: Retrieval of H_2O fraction in the 3^{rd} layer (3-D case). $E_{rms} = .5dB$. Parameters: $\theta_i = 40\,\text{deg}$, Amplitude $= 3cm$, $l = 20cm$, $\epsilon_{r1} = 5.5 + .3i$

and therefore it is important to make sure the inversion algorithm is robust enough to be effective. Figures 4.16- 4.18 demonstrate that the algorithm retains robustness in retrieval of the water content in the 3^{rd} layer. Since the parameters retrieved from the top interface are incorporated in developing closed-form equations relating subsurface parameters to backscattering coefficients, it is especially critical that the retrieval of these parameters be as accurate and robust as possible. To minimize the contribution of the subsurface, the simulation was performed at three L-band frequencies: 1000 MHz, 1100 MHz, and 1200 MHz. Figures 4.19 and 4.20 depict

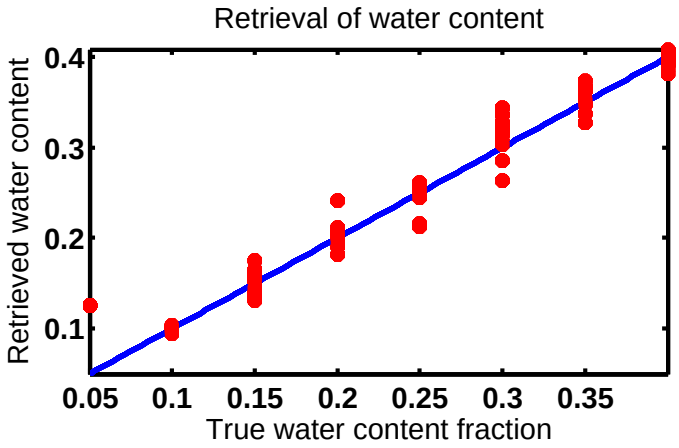

Figure 4.18: Retrieval of H_2O fraction in the 3^{rd} layer (3-D case). $E_{rms} = 1dB$. Parameters: $\theta_i = 40$ deg, Amplitude $= 3cm$, $l = 20cm$, $\epsilon_{r1} = 5.5 + .3i$

the retrieval of water fraction of the middle layer and amplitude of the periodic interface for the errorless case. With the data from the three measurement channels, the inversion results are very accurate and converge to a correct solution in every case. Figures 4.21- 4.23 depict the inversion results form the amplitude of the periodic interface when 0.1dB, 0.5dB and 1dB RMS error is introduced to the backscattering coefficients. As predicted the error in the retrieved amplitude increases with increased error in the backscattering coefficients but the algorithm retains robustness.

4.4 Conclusion

An efficient and robust algorithm for retrieval of parameters of interest from scattering coefficients is described in this chapter. The forward model is simulated for a range of parameters and the resulting data space is broken up into multiple subspaces and closed-formed representations are determined for each of the subspace. The conjugate gradient based inversion algorithm is applied to produce a solution in each individual subspace and the best solution is then picked out based on the magnitude of an appropriately defined cost function. The sensitivity of the algorithm to errors in ancillary parameters and scattering coefficients is carefully analyzed.

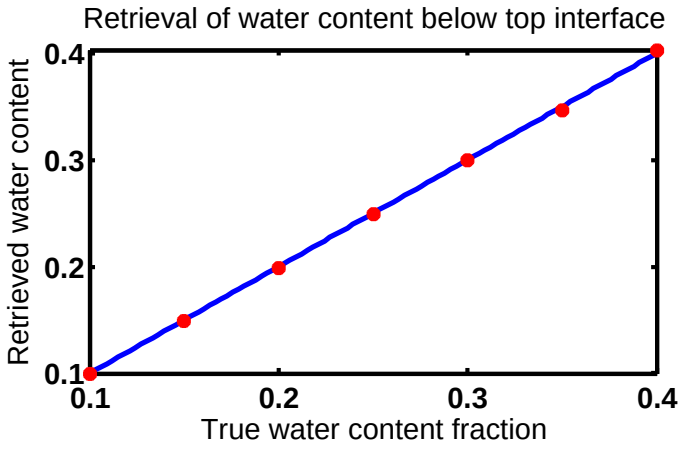

Figure 4.19: Retrieval of H_2O fraction in the 2^{nd} layer (3-D case). Parameters: $\theta_i = 40\,\text{deg}$, Amplitude $= 3cm$, $l = 20cm$, $\epsilon_{r1} = 5.5 + .3i$. Observation frequencies: 1000 MHz, 1100 MHz and 1200 MHz

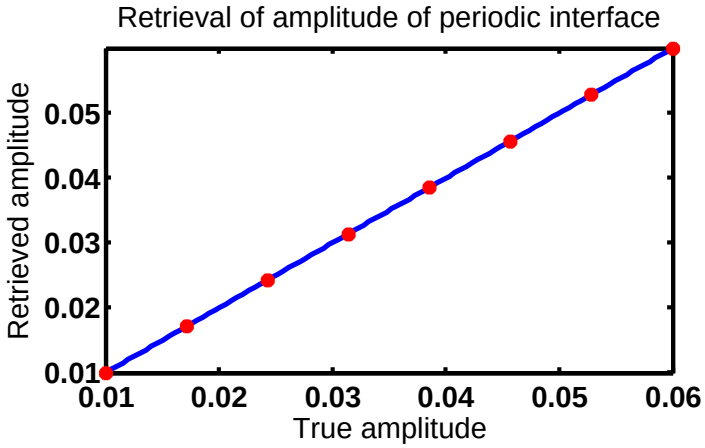

Figure 4.20: Retrieval of the amplitude of the periodic interface (2-D errorless case). Parameters: $\theta_i = 40\,\text{deg}$, $l = 20cm$, $\epsilon_{r1} = 5.5 + .3i$. Observation frequencies: 1000 MHz, 1100 MHz and 1200 MHz

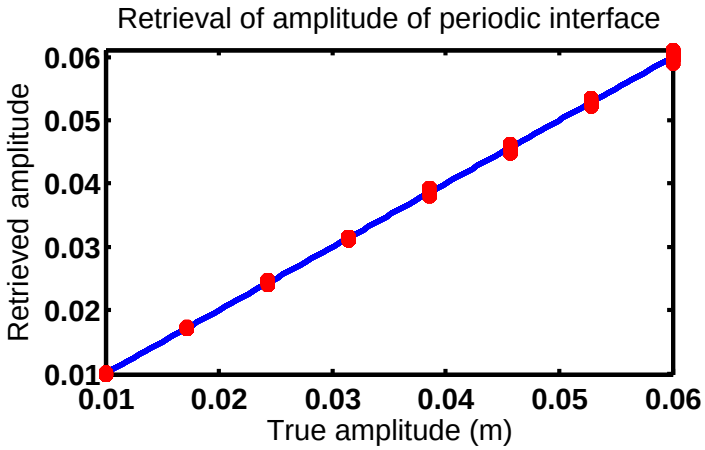

Figure 4.21: Retrieval of the amplitude of the periodic interface (2-D case). $E_{rms} = 0.1dB$. Parameters: $\theta_i = 40\,\text{deg}$, Amplitude $= 3cm$, $l = 20cm$, $\epsilon_{r1} = 5.5 + .3i$. Observation frequencies: 1000 MHz, 1100 MHz and 1200 MHz

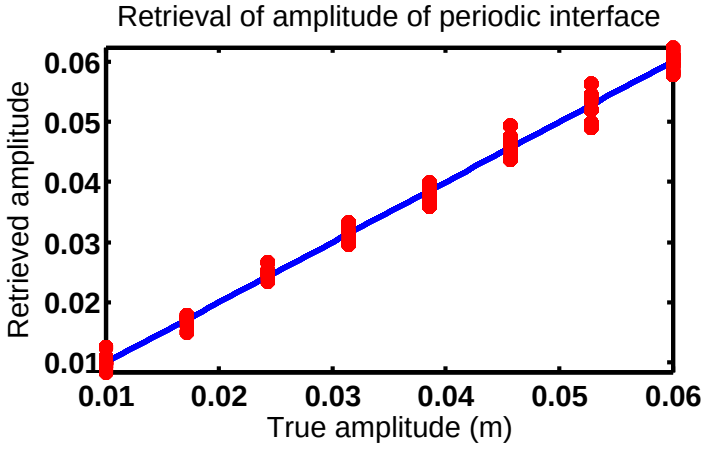

Figure 4.22: Retrieval of the amplitude of the periodic interface (2-D case). $E_{rms} = 0.5dB$. Parameters: $\theta_i = 40\,\text{deg}$, $l = 20cm$, $\epsilon_{r1} = 5.5 + .3i$. Observation frequencies: 1000 MHz, 1100 MHz and 1200 MHz

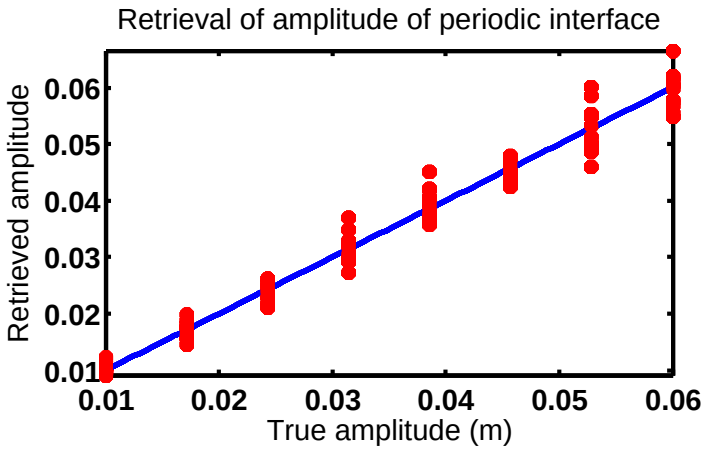

Figure 4.23: Retrieval of the amplitude of the periodic interface (2-D case). $E_{rms} = 1dB$. Parameters: $\theta_i = 40\,\text{deg}$, $l = 20cm$, $\epsilon_{r1} = 5.5 + .3i$. Observation frequencies: 1000 MHz, 1100 MHz and 1200 MHz

CHAPTER V

Multifrequency Tower Based Radar System for Forward and Inverse Model Validation

5.1 Introduction

This chapter is devoted to the description of two experimental radars developed to provide measurements of backscattering cross sections of media with nonsmooth interfaces. In addition to the radar hardware, advanced measurement and data processing techniques, measurement results, and validation using ground sensors are discussed in this chapter.

5.2 Radar Architecture

This section details the evolution of a radar system operating in the 120-1100 MHz range. A monostatic radar in this frequency range was originally developed at the Jet Propulsion Laboratory (JPL) (see [18]), which provided initial design and preliminary datasets. Over the course of several years the radar was modified and upgraded in search of an architecture that would produce the best quality measurements while having low cost and being conveniently deployed in the field. Finally, a new compact bistatic radar system was designed and built.

Figure 5.1: MOSS Radar picture. The system was a monostatic radar which used a large dual polarization log periodic antenna, balanced by a set of lead counterweights. The ground electronics consisted of (from the top) a signal generator, RF gound box, a computer housing a PCI digitizer, a radar power supply and an AC power backup unit

5.2.1 Modified MOSS Radar

This radar was originally designed and built at JPL to support the Microwave Observatory of Subcanopy and Subsurface (MOSS) project. It was one of the first tower-based systems capable of polarimetric measurements at 137 MHz, 435 MHz, and 1000 MHz frequencies. This radar was a pulsed continuous wave monostatic radar. The architecture of the radar is described in more detail in $A.1$. A picture of a tower and ground electronics is shown in Figure 5.1. The radar was involved in two exploratory measurement campaigns in Arizona and Oregon before being transported to Michigan. The radar suffered from several harware problems which degraded the quality of the measured signal.

Since the radar relied on solid-state switches for transmit/receive (T/R) switching, the power was limited to 21 dBm, the upper limit that these switches could with-

stand. These switches also have relatively poor isolation characteristics (∼30 dB), which results in unwanted transmit signals leaking into the receive chain during co-polarization measurements. This leakage signal arrived at the receiver at a different time than the expected receive signal and generally did not directly interfere with the quality of the measurement. This unwanted leakage signal, however, saturated the receiver and was approaching the maximum allowable power limit for receiver components, thus limiting the amplification that could be added to the receiver chain.

Another problem was that the radar was designed for receive signal levels that are about 60 dB below the transmit level. Typically, such a difference is only enough to detect very bright targets. Additionally, the log periodic antenna caused large reflections and pulse despersion. The impulse response of the dual-polarization log periodic antenna did not decay fast enough, and was still close in magnitude to the receive signal at the time window of the receive signal arrival. The antenna had a relatively poor (∼15 dB) polarization isolation and a wide, almost omnidirectional pattern in the E-plane. To address some of the shortcomings of the MOSS radar and to prepare the instrument for an experiment to estimate soil moisture under a corn canopy, the radar hardware underwent important modifications, explained in the next subsection.

5.2.2 Modified Bistatic MOSS Radar

To improve the hardware isolation between transmit and receive signals and to mitigate the effect of a long antenna impulse response, the radar was converted to a bistatic system, with the transmit and receive antennas connected to former H and V ports respectively. Since transmit and receive signals no longer pass through the same solid-state switch, the isolation is not limited by radar electronics, but by cross-coupling of the antennas. The antennas used in this version of the radar were high gain L-band Yagi-Uda antennas, which have a peak gain of 12 dBi and much narrower

Figure 5.2: A photo of the Bistatic Radar. Antennas are separated by a 6' custom made steel beam. The height of the tower is varried between 12m and 35m. The incidence angle is set manually for every antenna. In this picture the antennas are pointing up for calibration purposes.

beamwidths in both planes. Since Yagi-Uda antennas are narrow band resonant antennas, they similarly suffer from long impulse response times. To significantly dampen the ringing, the antennas were resistively loaded with 3 dB attenuators. Such loading decreases gain by decreasing antenna efficiency, but has no influence on beamwidth, thus preserving the spacial resolution. The new arrangement allowed for an addition of another amplifier in the receive chain to increase the expected difference between transmit and receive chain to about 70 dB. The modified bystatic system in the sky calibration state is depicted in Figure 5.2. The antennas are separated by a 6' steel beam. The incidence angle can be set for each antenna individually by rotating a disk at the end of the beam.

5.2.3 Compact Bistatic Radar

The most rapid changes in soil moisture occur during and right after rain events. In many applications of remotely sensing soil moisture, capturing rapid soil moisture

evolution associated with rain events is of particular interest. It is therefore impractical to use a system which can only be deployed in half a day. Since it was not possible to miniaturize the original MOSS radar, a new radar was designed and built. Table 5.1 summarizes the radar specifications to which it was designed.

Radar type	pulse
Pulse width	40-200 ns
Center frequency range	120 -1000 MHz
Peak Power	1 W
T/R difference	80-110 dB
Maximum weight	25 kg
Incidence angle selection	fully automated
Deployment time (2 people)	<1 hour

Table 5.1: The new radar specifications. The radar needed to be compact, easy to deploy and have superior RF characteristics than its predecessor

A detailed description of the new radar architecture is provided in $A.2$. Unlike its predecessors, the radar fits into a custom 1' by 1' by 2' aluminum enclosure. A standard 110 V extension cord is the only cable that connects to the system located atop the tower.

From radar theory, the range resolution of a radar is given by Equation 5.1. For 50 ns pulses the range resolution in air is approximately 7.5 m. Since the speed of light inside the dielectric is inversely proportional to $\sqrt{\epsilon_r}$, the resolution distance is shortened accordingly.

$$r = \frac{c_{medium}\tau}{2}, \tag{5.1}$$

where r is the range resolution in meters, c_{medium} is the speed of light in the medium in meters per second, and τ is the pulse width in seconds. To reach the best range resolution the pulse width has to be kept as short as possible. However, in practice, the minimum realizable pulse width is governed by the limitations of hardware (most fast solid state switches can generate pulses as short as 20 nS), impusle response of

the antenna and the amount of power radiated. To overcome the radiated power limitations, state of the art radar systems use long chirped pulses that can then be compressed to produce super range resolutions while radiating sufficient amounts of power. Unfortunately, chirp synthesizers and related hardware are very complex and were not in the budget for the current system.

The antenna choice for a low frequency pulsed system is one of the most difficult and important decisions the designer has to make. There are several conflicting requirements that the antennas have to meet. First, the gain should be large enough for good target isolation, as wide beamwidths pick up unwanted signals from the surroundings (tower, nearby objects). Second, the antenna impulse response should be as short as possible. Third, the antenna has to be of a practical size and weight.

5.3 Calibration

Calibration is one of the main technical challenges of the low-frequency radar development. The miniaturized radar used for this dissertation employs three types of calibration: internal, sky and target.

The performance of all electronic components is affected by changes in temperature. To minimize errors due to temperature variation, many state of the art systems use temperature controlled enclosures for their RF electronics. Temperature controlled enclosures are heavy, power hungry and expensive, so for this system an internal calibration measurement is used instead. To calibrate out the variations due to temperature changes, the electromechanical switches bypass the antenna, and instead route the signal through a load (80 dB fixed plus programmable attenuator combination) which attenuates the signal approximately to the level of the incoming receive signal. Internal calibrations are performed at the beginning and the end of every measurement, as well as every half an hour of measurement taking. Separate calibrations are necessary for every frequency channel. In addition to temperature

Figure 5.3: A typical setup for sky calibration. To minimize the capture of unwanted signals the antennas are pointing at 45° above horizontal.

calibration, internal calibration capabilities are an invaluable tool in troubleshooting and lab testing of the radar. Since the antennas are bypassed, work on the radar can be performed in any lab and does not require an anechoic chamber.

One of the biggest challenges in building a low frequency radar is finding a compact antenna with a short impulse response. If the antenna impulse response in the measurement time window is repeatable and does not saturate the receive-path electronics, it can be calibrated out. The calibration procedure employed to remove the antenna response is called a sky calibration. In order to perform this calibration the antennas are rotated to point at 45° above horizontal and the data trace is recorded. Pointing the antennas straight up produces more error since the back lobe of the antenna captures a strong ground specular return. The sky calibration trace is then substraced from all subsequent data traces. Figure 5.3 depicts the radar mounted on the tower with antennas in the sky calibration position.

Another form of calibration explored in this work is a standard target calibration. The standard target calibration involves placing a target with a known radar cross section in the radar footprint and measuring the received signal. Since the cross section of the target is known, this measurement allows for absolute radar calibration. One of the dfficulties of this meathod is to isolate the response of the standard target

from the response of the surroundings. At high frequencies, a good degree of isolation can be achived if this measurement is performed in the anachoic chamber. Figure 5.4 shows a 1 GHz calibration getting performed in the University of Michigan anechoic chamber. A corner reflector and the radar are placed at the opposite ends of the chamber and the distance between them is carefully measured using a laser range finder.

Most anechoic chambers have a cutoff frequency in the UHF range and are not suited for VHF standard target calibration. Moreover, at VHF frequencies the targets become too large to fit inside most chambers. Typical standard targets are metalic spheres, plates and corner reflectors. It is worth noting that exact analytical expressions for the radar cross section are only availible for the sphere. The approximate cross section equations for the metal plate and corner reflector are only valid when the size of the target is large compared to the wavelength. Sphere calibration targets are typically used in chamber tests at high frequency since their relatively low brightness increases the relative contribution of the surroundings. Metalic plates are the simplest targets to manufacture but are rarely used due to the required alignment tolerances. Even a slight (less than 1°) misalignment is enough to render the measurement useless.

Large corner reflectors (more than 5λ) are often a preferred radar calibration target due to their strong brightness and very lax alignment requirements. The radar cross section is given by equation 5.2, making it one of the brightest targets relative to its size. Moreover, the radar cross section of a large trihedral corner reflector is approximately independant of the incidence angle over a wide angular range.

$$\sigma_{CR} = \frac{4\pi}{3}\frac{l^4}{\lambda^2} \tag{5.2}$$

The target used for most outdoor testing was an 8' trihedral corner reflector.

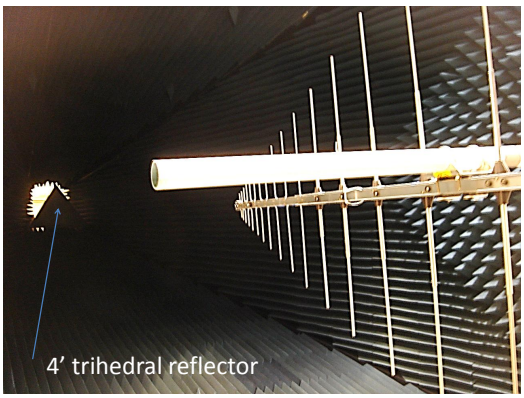

Figure 5.4: Calibration inside anechoic chamber. At high frequencies accurate absolute calibration can be performed inside the anachoic chamber. Here the measurement is done at 1 GHz. At lower frequencies the chamber attenuation characteristics significantly deteriorate.

The reflector can be easily taken apart for transporation and redeployment. While the reflector is large enough to meet the approximation requrement at L-band, it is still only slightly over a wavelength at VHF. For L-band measurements at low tower height, the corner reflector response saturates the receiver and makes it impossible to obtain an absolute amplitude calibration. However, the measurement is still valuable for providing a precise time calibration. At higher tower elevations the corner reflector allows for absolute amplitude calibration for L-band frequencies. At lower frequencies the cross section becomes sensitive to incidence angle, such that even a slight misalignment results in 2-3 dB change in observed cross section. Moreover, the expressions for the magnitude of the cross section of the corner reflecor are no longer valid at VHF. Therefore, accurate standard target calibration at VHF frequencies is still an open problem.

5.4 Measurement and Data Processing

Typically, each data campaign contains hundreds of individual measurements. These measurements include data takes over different days to detect change, data taken at different frequencies and incidence angles, sky calibration takes and special

calibration measurements when a known target is placed in the footprint of the radar antenna. A typical data set contains an internal calibration measurement, one or two sky calibration measurements and tens of data measurements. After mounting the hardware, raising the tower to the upright position and establishing a wireless connection between the radar and the ground computer, the operator lets the radar temperature stabilize and reach equilibrium. A temperature sensor mounted inside the radar box monitors the temperature during the entire measurement cycle. Once equilibrium is reached, several internal calibrations are performed to make sure the radar is stable and ready for measurement. Then, a sky calibration is performed by recording the data while the antenna is pointing at the sky. Measurement data is collected by pointing the antenna at the target and recording the data. The height of the radar is accurately provided by a laser range finder. The tower is then raised by some increment and the process is repeated. Typically, another sky and internal calibration data takes are done at the end of every data set.

Generally, high gain antennas tend to be electrically large (several λ long) which leads to impractically large size and weight for the antennas working at VHF frequencies. Antennas of practical size have wide beamwidth, and therefore large footprints. To reduce the footprint (and therefore improve the resolution) and to increase the signal to noise ratio, a coherent beam focusing algorithm was applied in post processing to the radar data. The focusing algorithm is based on the antenna array theory - data traces are shifted to account for the path difference between measurements. As a result, the gain of the synthetic antenna is approximately equal to the product of the gain of the actual antenna and the gain of an array of isotropic radiators located at the points of measurement. The schematic footprint reduction is illustrated in Figure 5.5. By adding differnet phase shifts, the beam can be focused at different points along the line perpendicular to the antenna mount. Since focusing relies on accurate phase information, it can only be performed when working with I and Q data before

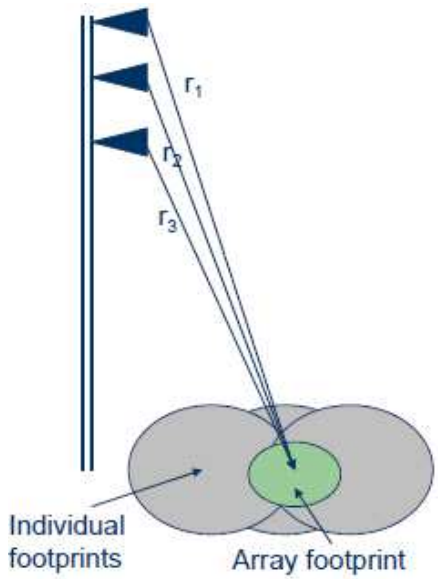

Figure 5.5: Schematic effect of focusing. The beam is significantly sharpened by coherent additions of individual data traces.

it is converted to power.

5.5 Radar Data Validation

The performance of the radar instruments is typically validated by placing in situ sensors in or near the footprint of the instrument. To confirm sensitivity of the radar instrument to changes in soil moisture, the local soil moisture sensors supplied by Decagon devices were chosen for this purpose. These sensors, pictured in Figure 5.8, operate by measuring the change in capacitance between the prongs. EC 5 sensor is an inexpensive soil moisure sensor that can be easily integrated with a custom data aquisition device and logger. The interface for each probe consisted of three wires: supply, signal and ground. When ON, the device is powered by a DC voltage in the range between 2.5 and 5 V. The singnal wire outputs a DC voltage which is proportional to the moisture content of the soil. Since many of the radar measurements were performed at the Matthaei Botanical Gardens' community

Figure 5.6: USB 8 channel data aquisition module. This inexpensive module combines 8 analog channels and 16 bi-directional digital lines. Three modules were necessary to sample the signal from the 22 sensors

garden, two identical 1.5 m holes were dug near the community garden and used to install 11 sensors in each hole. Two identical installations were chosen to estimate the variations of sensor measuremnts at the same depth and to provide redundancy in case of sensor failure. Since soil moisture typically varies faster near the surface, the sensors were installed more densely there. The sensor locations are depicted in Figure 5.7.

A custom data logger was contructed to collect data from the 22 sensors. An old desktop computer was placed in a shed about 25' from the deployment site. All the power and ground wires for the probes were connected to a thick cable (for low resistance) and to 5V and Gnd terminals of the computer power supply. The signal wires are connected to 2 multiconductor cables which are run into the shed. The voltages are sampled by three 8-channel USB data aquisition modules depicted in Figure 5.6 and the data is stored in the computer. Sensors were pushed horizontally into the undisturbed soil to minimize the disruption of the natural soil texture, as soil density affects sensor readings. To obtain meaningful soil moisture readings, the sensors need to be carefully calibrated.

The calibration procedure involves collecting a soil sample and carefully heating it at very low heat to evaporate the water. The sample is then carefully weighted. The reading from the soil moisture sensor is recorded for 0 % water content. The amount of water necessary to increase the water content to the desired incremental

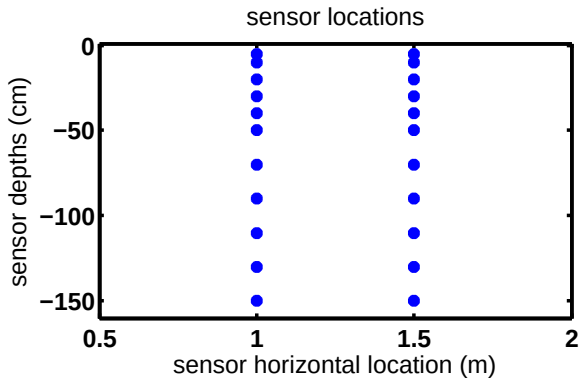

Figure 5.7: Soil moisture sensor locations. Two idential columns of sensors were installed to estimate sensor reading variability and to introduce redundancy in the case of sensor failure.

Figure 5.8: Decagon Devices soil moisture sensor.

value is added to the soil and carefully and thoroughly mixed in. The reading from the sensor is recorded and the process is repeated until soil saturation is reached.

Once the data was collected, closed-form functions are fitted to the data to obtain analytical expressions relating the readings of each of the sensors to the soil water content. From several experiments 3^{rd} order polynomials produce the best compromise between accuracy (with fit errors $< 1\%$) and simplicity of the expressions. Figure 5.9 depicts a calibration curve for one of the soil samples collected and 5V excitation voltage. Equation 5.3 relates sensor voltage measurements to the gravimetric water content.

$$f_{H2O} = 1.1242V^3 - 3.5356V^2 + 3.9765V - 1.4326 \tag{5.3}$$

Once the true soil moisture is computed from the voltage measurements of the in-situ sensors, the data must be converted to dielectric constants. There are a number

	$3V$ Excitation		$4V$ Excitation		$5V$ Excitation	
Gravimetric $\frac{m^3}{m^3}$	sensor 1	sensor 2	sensor 1	sensor 2	sensor 1	sensor 2
air	.285	0.294	0.401	0.394	0.478	0.482
0%	0.421	0.42	0.568	0.57	0.697	0.695
2.50%	0.456	0.46	0.603	0.599	0.733	0.726
5%	0.492	0.512	0.641	0.655	0.772	0.789
7.50%	0.521	0.543	0.667	0.685	0.804	0.827
10%	0.555	0.576	0.699	0.725	0.848	0.908
12.50%	0.586	0.594	0.74	0.755	0.922	0.945
15%	0.645	0.658	0.855	0.884	1.055	1.067
17.50%	0.796	0.794	1.007	0.99	1.216	1.183
20%	0.767	0.805	0.984	1.001	1.182	1.203

Table 5.2: Typical sensor calibration measurements. Typically two sensors are used to make sure the samples are well mixed. A large difference between the readings would point to poor mixing and non-uniform samples.

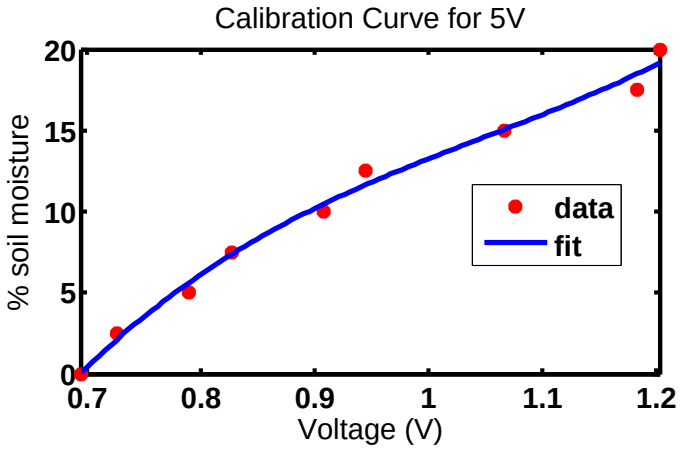

Figure 5.9: Calibration curve for 5V excitation. After calibration coefficients are determined, the readings from the sensor can be immediately converted to moisture content

of dielectric models available and the one used in this work is described in [30]. The model predicts the dielectric constant of a soil based on soil composition (sand, clay and silt fractions), bulk density of the soil and water content. The soil encountered at the Matthaei Botanical garden can be modeled as a two layer structure with a clay dominated layer on top of a sandy layer.

5.6 Radar Data

The data from several measurement campaigns is presented in this chapter. Figure 5.10 shows the focused data from several data takes measured at L-band center frequency by the bistatic L-band radar described in 5.2.2. One of the measurements was performed shortly after a heavy rainstorm passed through the area. As can be clearly seen, there is a noticeable difference between the after-rain trace and all other traces taken when the soil was drying up. However, the cross section data could not be successfully corroborated with the readings of the in situ soil sensor in this measurement. The radar footprint was a freshly plowed corn field before the plants emerged from the ground. Careful measurements were performed of the soil-air profile. It is quite likely that the heavy rain that caused the noticable soil moisture change also altered the statistical properties of the air-soil interface.

Several data sets were collected in Ann Arbor during Spring of 2011. Figure 5.11 shows a typical raw data trace for L-band data. The sampling rate for each channel is 1 Gs/s. The former and the latter 1000 samples represent I and Q channels respectively. The data was sampled with an 8-bit ADC with 0 corresponding to -1V, 255 to 1 V and 128 to 0 V. Figure 5.12 shows two plots taken in May 2011 in Ann Arbor, MI about 1 week apart. The graphs show relative values of received power vs. time. To estimate the difference in cross sections, the power values were integrated over the receive window, converted to dB scale and subtracted. The result is the cross section difference observed between two different data takes. The difference in

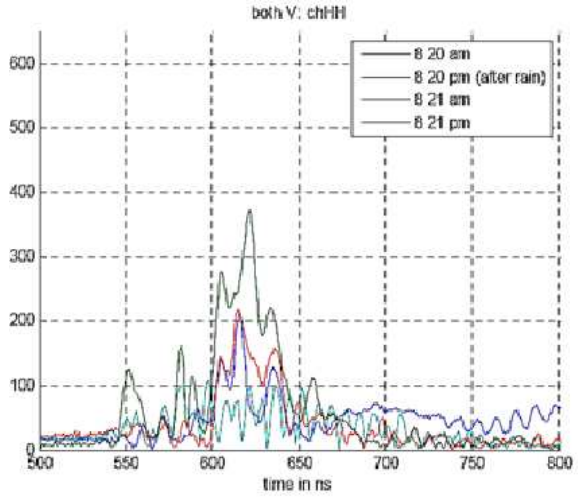

Figure 5.10: Data from the modified bistatic radar. Radar traces taken before and after rain: the trace collected after the rain storm is noticeably different from the 'dry' measurements.

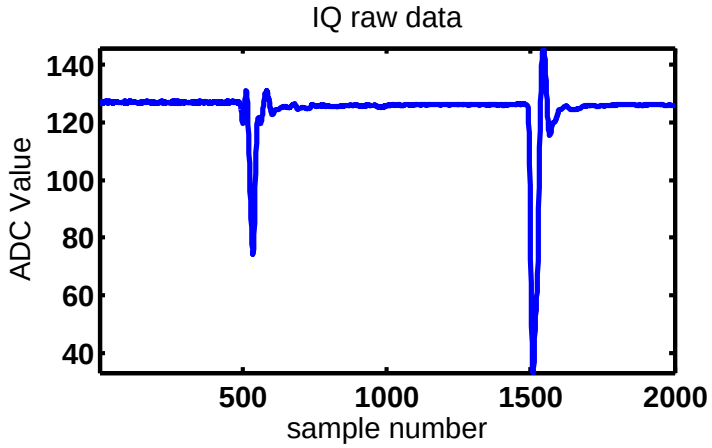

Figure 5.11: Raw IQ data collected by ADC card. Two channels (I and Q) are given in succession

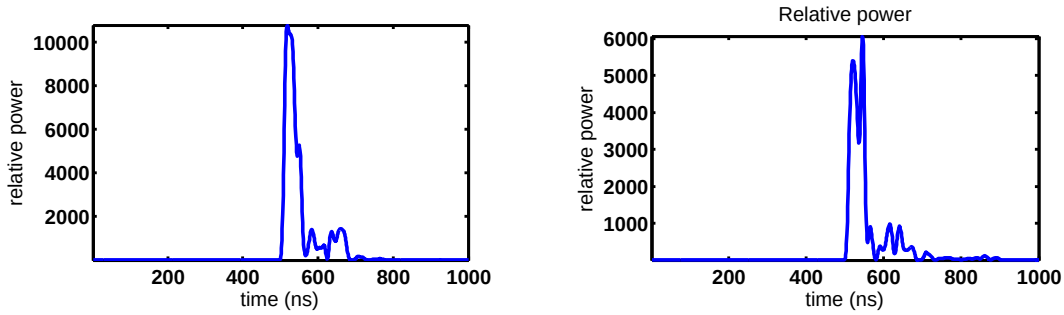

Figure 5.12: Michigan 2011 L-band data for wet and dry soil. The y axis shows power obtained by combining I and Q processed measurements. Since only relatve power is important, the measurements are not magnitude calibrated

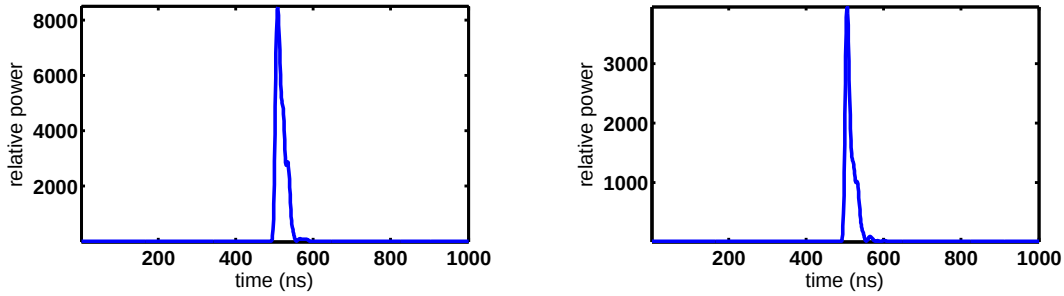

Figure 5.13: Florida June 2011 L-band data for wet and dry soil. The y axis shows power obtained by combining I and Q processed measurements. Since only relatve power is important, the measurements are not magnitude calibrated

this case is approximately 2.6 dB. Using Peplinsky-Ulaby-Dobson model and EBCM forward model, the predicted difference should be 3.4 dB.

Figure 5.13 shows the results of a similar experiment conducted in Florida in June 2011. This time the measurements were taken only about 12 hours apart but one of the measurements was of dry soil and the other of a soil after a heavy thundrestorm. A similar procedure was undertaken to estimate the difference in cross section to be 4.3 dB.

The experiment was repeated at UHF (435 MHz) frequency to compare with the results for the L-band. Figure 5.14 shows comparision between measurements of wet and dry soil. The relative cross section difference derived from the power graphs is

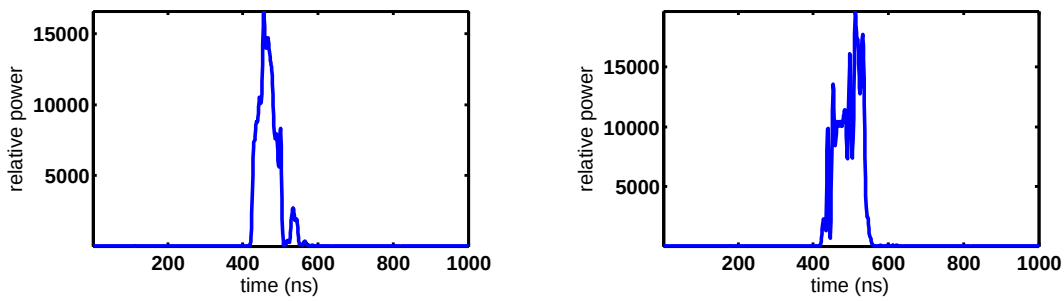

Figure 5.14: Florida June 2011 P-band data for wet and dry soil.

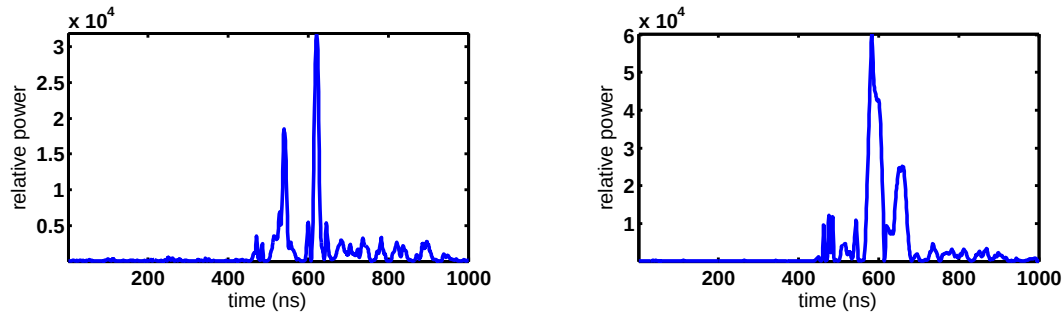

Figure 5.15: Michigan VHF data. At VHF frequencies the radar data shows greater descreptancy with the values derived from the in situ sensor readings

estimated to be 1.47 dB. Figure 5.15 shows the relative received power graphs for VHF (137 MHz) measurements. The difference derived from the radar data is about 4.2 dB. The predicted difference from the model is only .61 dB. The difference can be attributed to a number of factors: dielectric models used to convert moisture fraction to dielectric constant are only valid above 300 MHz; the radar antennas perform the worst at low frequencies; the contribution of the subsurface is more important and therefore the errors in the ancillary parameters (surface roughness, depth of the subsurface layer, etc) play a more important role.

5.7 Sources of Error in Measurement and Validation

Since both radar data collection and ground truth validation processes contain errors, it is important to carefully identify and characterize all the important sources

of error. Major sources of error include:

- variability in the electronics
- imperfect sky calibration
- contributions of the surroundings
- modeling errors
- errors in measuring ancillary parameters
- imperfect dielectric models and model input parameters
- ground sensor measurements not representing true means

The behavior of all electronic components varies to some degree from one measurement to the next. In the case of radar electronics, the variability is most pronounced in the behavior of solid-state switches that have a typical rise time of 10 ns and are typically used to create 40-60 ns pulses. The variability between two individual traces can be significant and is mitigated by averaging the receive signal over hundreds of measurements. There is also variability in measurements due to different temperature, huminidty and other environmental factors. When the measurements are averaged and proper internal calibration procedures are applied, the errors due to electronics are significantly smaller than other sources of error.

Sky calibration records the data when radar antennas are pointed at the sky and not at the target. Ideally, the receive signal is purely antenna impulse and cross coupling responses, which can be calibrated out from subsequent traces. There are two sources of error in sky calibration: phase instability in cables and side/back lobes of the antenna. When antennas are rotated to point at the sky, transmit and receive cables are bent introducing errors due to changes in propagation properties of the cables. When antennas are pointing at the sky, the side lobes still pick up signals from the ground, tower and other objects. The quality of a sky calibration is limited by side-lobe level of transmit and receive antennas.

To stay within practical size and weight limits, low frequency radars use relatively

low gain antennas, resulting in unwanted radiation into the surroundings. The receive signal includes not only scattered signals by the target but also signals picked up from the surroundings. As with the sky calibration case, the quality of the measurements is degraded by the side and back lobes. However, unlike the sky calibration, this problem can be partically solved through coherrent focusing techniques.

Even though the three-layer model presented in this dissertation is more accurate and appropriate than previously used single rough-interface models, it is still an approximation of the actual media. The model assumes homogeneous layers with clear boundaries between them. In reality soils are multilayered inhomogeneous structures with inclusions of various shapes and sizes and no clear boundaries between the layers.

Errors in ancillary parameters is another serious source of discreptancy between predicted and measured variation of the dielectric constant. While quantities pertaining to the first interface can be measured or visually approximated with high degree of accuracy, there is no easy way to accurately obtain subsurface parameters. Approximate values are obtained by inspecting sides of several holes dug for this purpose.

The dielectric model used to relate soil moisture to dielectric constant was only developed for measurement frequencies above 300 MHz and the accuracy of the model at VHF frequencies is not known. Moreover, sand and clay fractions and soil density are also model parameters which are not easy to accurately measure. Errors in the model parameters could produce highly erroneous estimates for the dielectric constant of the soil.

Another potential source of error is the difference between ground sensor measurements and the true mean of the radar footprint. Since ground sensors are expensive to install only two validation sites were established.

In order to successfully validate forward and inverse scattering models, it is important to develop techniques to address the above mentioned sources of error.

5.8 Conclusion

In this chapter a summary of the experimental part of the dissertation is presented. Three radar instruments were either modified or built for experiments in soil moisture estimation. Significant progress was made in improving the performace of the radar instruments, miniturization and shortening of the deployment times. Radar data processing algorithms were developed to improve the quality of the signal and reduce the antenna size necessary for successful soil moisture estimation. An in-situ sensor network was installed and calibrated to validate radar measurements. A clear relationship was established between a change in magnitude of the radar return and the observed changes in soil moisuture. To further improve the instruments, more work needs to be done on obtaining a compact wideband non-dispersive antenna and finding a compact signal generator with performace characteristics similar to laboratory signal generators. Additionally, substantial amount of work remains to be done in the area of improving radar data validation.

CHAPTER VI

Conclusion and Future Work

6.1 Dissertation Summary

The goal of this thesis was to develop efficient forward and inverse scattering models, and then design and build a radar instrument which could be used to validate these models. First, an efficient and accurate forward scattering model based on EBCM and the scattering matrix technique was developed for a three layer medium. The boundary between the 1^{st} and the 2^{nd} layers of the medium is periodic and there is a random rough interface between the 2^{nd} and the 3^{rd} layers. Typical forward scattering models represent the 1^{st} interface as a random rough surface. For many types of media, such as fresh bodies of water and plowed agricultural fields, the periodic on top of rough model is more appropriate than most other forward scattering models. Next, the forward model is extended by including a cylinder with an arbitrary cross section embedded in the 3^{rd} layer. This particular forward model is especially applicable to detection of buried objects and through the wall imaging. The inverse scattering model presented in this dissertation is a local optimizer based on the modified conjugate gradient method. To cast the forward model into a form fit for inversion, the forward scattering model is simulated over large domains of values to obtain closed form, analytically differentiable relations. The total simulated data space is broken up into smaller subspaces, and the problem is solved for every individual subspace. The

best solution is then chosen based on the magnitude of the cost function. Since the computational complexity strongly depends on the number of parameters to retrieve, the model is simulated at high frequency to isolate retrieval of parameters pertaining to the top interface followed by the simulation at lower frequency to retrieve the rest of parameters. Error analysis demonstrates the robustness of the proposed method to added noise by showing that the average values of inversion results do converge to the actual values. To confirm the utility of the forward and inverse scattering models a novel, compact radar instrument was designed and manufactured. The system is efficient and partially automated for rapid data collection. Using a coherent focusing algorithm, a relationship between cross section coefficients and soil moisture was established, however the validation of forward and inverse scattering models was not complete.

6.2 Future Work

6.2.1 Forward Scattering Model Enhancement

The forward scattering model presented in this dissertation accurately represents many naturally occuring and anthopogenical media such as fresh bodies of water, plowed agricultural fields, walls, etc. One challenge for remote soil moisture estimation is vegetation modeling. While short grassy vegetation is nearly transparent to VHF/UHF bands, forests layers (including roots) cannot be ignored. The current forward scattering model can be significantly enhanced by integrating it with tree models (cite Mariko's work) to develop a complete forward scattering model for a forest. There is also a need to increase the region of validity and computational efficiency of the current forward scattering model. A recent work on stabilizing the 3D EBCM presented in [31] shows promising preliminary results in extending the region of valitity of the algorithm. A similar technique, if developed for a two dimensional

version, could significantly increase the region of validity of the model.

6.2.2 Scattering from 2D cylinder

In this dissertation an efficient forward scattering model for an arbitrary two dimensional cylinder behind a non-smooth wall was developed. The model combined a reflection matrix for a cylinder derived from the MOM formulation with reflection and transmission matrices derived for periodic and rough interfaces using EBCM. The MOM algorithm used the simplest uniform rectangular integration technique, resulting in a relatively fine discretization requirements, especially for non-smooth cylinders and TE polarization. A more sophisticated MOM algorithm would allow for a significant reduction in the number of segments per wavelenth, and improvement in the efficiency of the algorithm. The model was validated by comparison with theoretical results obtained for a circular cylinder. Since a circular cylinder is a symmetric and smooth shape, more validation is desirable for rigorous method evaluation. The next step would be to experimentally confirm the model by measuring scattered fields for various wall types and cylinder shape combinations.

6.2.3 Retrieval of Parameters

The inversion algorithm proposed in this work is an efficient local optimizer based on a modified conjugate gradient method. The results for retrieval of parameters for three layer media were presented in this dissertation. The algorithm can be further extended to include retrieval of the cylinder parameters, so it can be used along with a measurement setup for through-the- wall applications. Since the most computationally complex step is the initial simulation over the range of parameters, once closed form expressions are derived, all subsequent computations are simple matrix evaluations. It may be promising to take advantage of computational efficiency of the closed form expressions to test the feasibility of using a global inversion algorithm

such as simulated annealing. Better results may be obtained at a modest increase of computational complexity.

6.2.4 Tower-Based Radar System Future Improvement

The radar instrument designed and built as part of this work is one of the first compact tower-based low frequency systems of its kind. There are several potential areas of advancement of these types of instruments. The most urgent is development of a compact low frequency antenna with a short impulse response. Recently, promising early results were reported in [32]. There is also an ongoing search for a compact quality frequency synthesizer. One possibility would be to design and build it at ourselves to ensure proper integration with the rest of the radar hardware. On the measurement side, there is a need to conduct an experiment to validate the inverse scattering models proposed in this dissertation. In order to take advantage of the penetrating abilities of the low frequency radiation, many of the subsurface measurements need to be performed at VHF (137 MHz) frequencies. However, the current dielectric model presented in [30] is only valid above 300 MHz. There is a need to extend this model down to VHF frequencies to accurately relate soil moisture, density and composition to the dielectric constant. Finally, there are several more experimental systems currently being considered. One of the systems currently in the proposal stage is a compact (under 22 lb) radar mounted on an unmanned aerial vehicle.

APPENDICES

APPENDIX A

Radar Architecture Description

A.1 Modified MOSS Radar

The schematic of the original MOSS radar is depicted on figure A.1. The computer controlled signal generator generates a continuous wave, which is then split into two branches by a 10:1 directional coupler. The larger signal (90% of the power) goes to the IQ demodulator to provide the Local Oscillator (LO) signal for the received Radio Frequency (RF) signal. The coupled in 10 % signal is then taken through two solid state switches. The switches stay on only for a few nanoseconds (typically 50 ns) at a time to produce pulses narrow enough for sufficient range resolution (see 5.2.3 for discussion of relationship between range resolution and pusle width). The signal then travels along the long RF cables to the component box located at the top of the tower. The signal there is amplified to about 21 dBm (signal generator is typically set to output +15 dBm of RF power) and passes through another solid state switch which acts as a duplexer switching between the transmit and receive paths. Since a PC serial interface cannot achive timing control on the ns scale all time critical signals are generated by the FPGA.

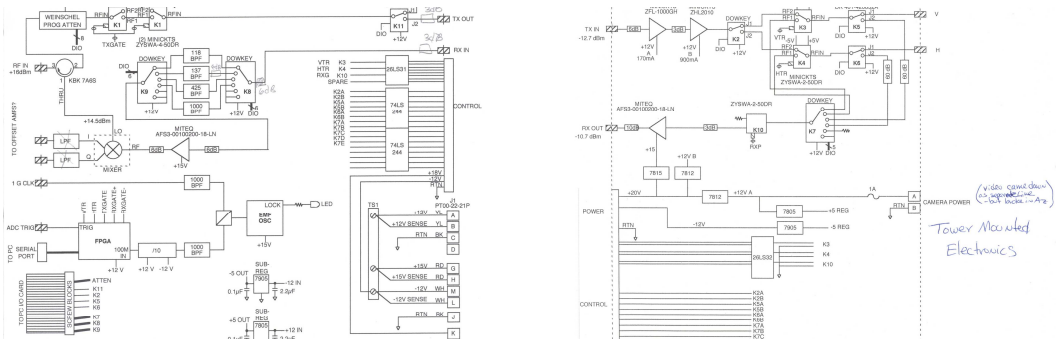

Figure A.1: MOSS Radar simplified schematic. The system was one of the first pulsed multi-frequency tower based systems built for soil moisture surveying. One of the main drawbacks of the system was a separate electronics box at the top of the tower, requiring the use of two RF and one multi-conductor power cables. This arrangement resulted in long deployment times.

The radar has two measurement channels: H (for Horizontal polarization) and V (for Vertical polarization). A set of electromechanical switches controls the choice of transmit and receive polarizations (with HH, HV, VH and VV being the possibilities). The transmit signal is then radiated from the antenna, and after scattering from the target, is received by the same antenna. The antenna used for this radar is a dual polarization log periodic antenna. It is mounted on a long aluminum pole with two circular hoops (connected with several bolts) at one end, and two lead counterweights at the other end. The incidence angle is set by unbolting the connection at the hoops and rotating the antenna. The receive signal captured by the antenna is then amplified by the Low Noise Amplifier (LNA), travelled down the RF cable back to the ground electronics box where it is mixed down to baseband and sampled by the computer based digitizer.

A.2 Compact Bistatic Radar

In order to significantly simplify the design and reduce cost, the system relied on many widely used and extensively tested off-the-shelf devices. The operating system

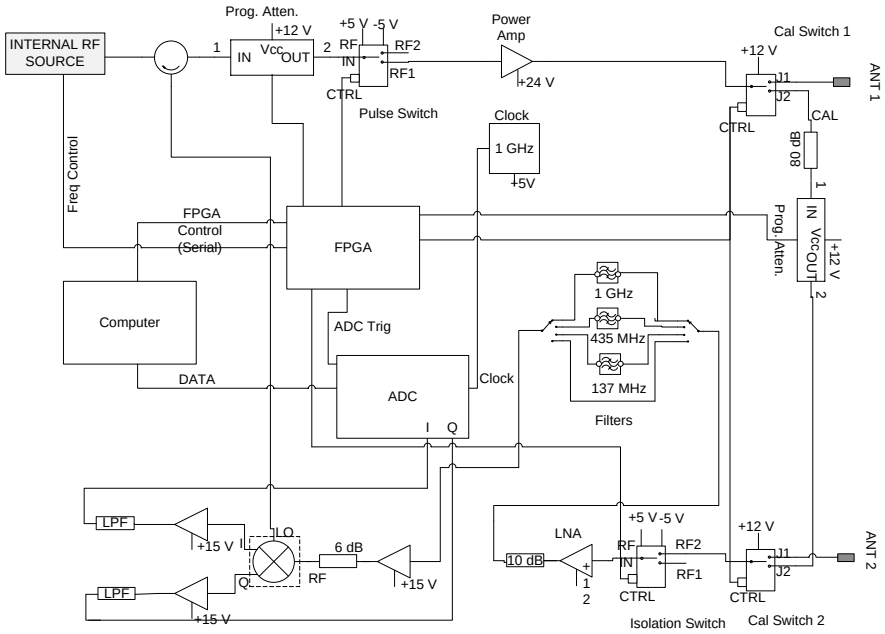

Figure A.2: The new compact radar simplified schematic.

is a standard Windows XP operating system which includes many built in features such as serial communication and peer to peer wireless networking. The hardware running the operating system is a small form factor, low power, fanless Intel ATI motherboard/processor/video card integrated system. The radar control and data aquisition program (written in LabVIEW) communicates with the rest of the system using serial protocol via the COM 1 connector on the motherboard. Serial commands that are generated by the computer are transmitted to an FPGA Spartan II board which generates control signals for most of the RF components. A simplified radar schematic is given on figure A.2. The RF signal is generated by a frequency synthesizer built by General Electronic Devices. The RF source has a voltage controlled oscillator in the range of 1-2 GHz and several dividers providing an output signal in the range of 100Mhz to 1.5 GHz at approximately 10 dBm of RF power. The control is executed via a 25 pin parallel connector with custom pinout. In addition to providing 15V

of DC power, there are three combinational circuit lines which set the values for the dividers. Also, there are clock, data and latch pins which set output frequency of the voltage controlled oscillator. The RF performance of the source is inferior to the signal generator stand alone instrument used in previous radars but the size of the RF source (3" by 3") makes it an attractive option.

The continuous wave signal generated by the RF source is split in a 10:1 ratio by a directional coupler. The larger signal becomes an LO signal of the IQ demodulator, and the smaller signal is passed though the solid state switch which generates a pulsed signal. The pulse is then amplified by the power amplifier and radiated by the antenna. Just as the previous versions, this radar is equipped with an internal calibration feature. The internal calibration is implemented with two electromechanical switches which bypass the antennas and instead route the signal though an attenuator of the magnitude similar to the attenuation between transmit and receive signals. Unlike the previous version, the attenuation can be adjusted to imitate a wide variety of targets. The minimum attenuation is set at 80 dB.

Even if the antennas are separated by the maximum allowable distance, the largest receive signal comes from the cross coupling between the transmit and receive antennas. This signal saturates the receiver, and can damage sensitive electronic components. To protect the receiver, a solid state isolation switch is used. It connects the receiver to the receive antenna a few nanoseconds after the cross coupling signal had passed. For small tower heights, this delay is set conservatively to ensure the capture of the wanted signal. For larger tower heights, the target response and the coupling response can be more easily separated.

The solid state switches used for isolation introduce a video leakage noise, which after amplification by LNAs can saturate the receiver. The spectral content of this noise is almost exclusively below the frequencies of the desired signal, which make it possible to remove most of this noise with bandpass filters. For higher frequency

measurements the removal of the video leakage noise is more complete.

After the receive signal passes through the isolation switch it is amplified, filtered, amplified again and is demodulated to baseband by an IQ demodulator. For superior noise performance it is important to place the low noise amplifier as early in the receive chain as possible. This radar uses an amplifier with a noise figure of 3 and around 40 dB of gain across the entire frequency band. Since the phase information is critical for focusing and data processing operation the use of an IQ demodulator is preferred to a standard RF mixer. The IQ demodulator splits the RF signal into two branches: the first branch is mixed down and produces the in-phase component (I), while the other is shifted 90° prior to down converting producing a quadrature (Q) component. The resultant channels are amplified by the baseband amplifier and filtered by a pair of lowpass filters to remove LO and higher order harmonics. From the noise performance point of view, it is preferable to avoid mixing the signal down to baseband, since the phase noise of the RF source is amplified. On the other hand, the superior from the noise performance point of view method of mixing to the intermediate frequency (IF) significantly complicates the radar hardware. The filtered I and Q channels are sampled by the digitizer at 1 GS/s and the data is stored on the computer hardrive.

The antennas used for this system are two identical log periodic antennas with a bandwidth of 100 - 1300 MHz ($S_{11} < 10dB$). The antennas are about 4' long (a relatively small size for VHF antenna) and provide a free space gain of 8 dBi. The antennas are mounted on a 10' aluminum pole using u-brackets. The separation between the antennas can be adjusted from 4' to almost 10'. The pole holding the antennas is inserted into the antenna rotator depicted on figure A.3 and secured with two u-bolt clamps. Both the rotator and the radar are mounted on a 5' by 1' aluminum plate. To prevent the plate from bending, the plate is reinforced at the edges by u-shaped rails. The plate holding the radar and the rotator is attached to

the tower by 4 bolts spaced by exactly 90°. This allows for 4 possible measurement directions (front, back and sides of the tower).

The incidence angle is set by turning the boom on which the antennas are mounted. The rotator (Yaesu 550) provides a 6 pin connector for the controller interface. The schematic of the motor is shown on figure A.3. The motor is rotated clockwise if 29V AC is applied between pins 4 and 6 and counterclockwise if applied between 5 and 6. The motor provides position feedback via a built in potentiometer. If DC voltage is applied between pins 1 and 3, the voltage between pins 1 and 2 is proportional to the position of the rotator. A custom rotator controller was designed and built to remotely set the antenna incidence angle. The rotator controller simplified schematic is schown on figure A.4. A step down fused transformer was used to obtain the 29V AC signal needed for antenna rotation. The signal is connected to pin 4 or 5 via a voltage activated AC relay depending on the desired direction of rotation. A USB based DAQ was used to sample the voltage at pin 2 and to actuate relays. A system was carefully calibrated by accurately measuring a voltage at $-178°$, $-90°$, $0°$, $90°$ and $178°$ and fitting a polynomial function which maps voltage to angular position. When the system powers up, it is theoretically possible that some residual charges could turn on both relays and try to rotate the motor in both directions simultaneously. To avoid this dangerous situation, large pull-down resisters were inserted between the gate terminal and ground of each relay. When nothing is written to the digital output lines of the controller, these resistors force the voltage at the gate of the relays to 0V, turning off the relays. Whenever nanosecond switching speed is not necessary, electromechanical switches are preferred due to their superior RF characteristics. Electromechanical switches are wideband (with VSWR values very close to 1), can handle high power levels (up to kW), and are essentially lossless. Solid state switches generally have an insertion loss of .5 - 2 dB, and can only safely handle about 23 dBm of RF power. Video leakage is another major problem at low

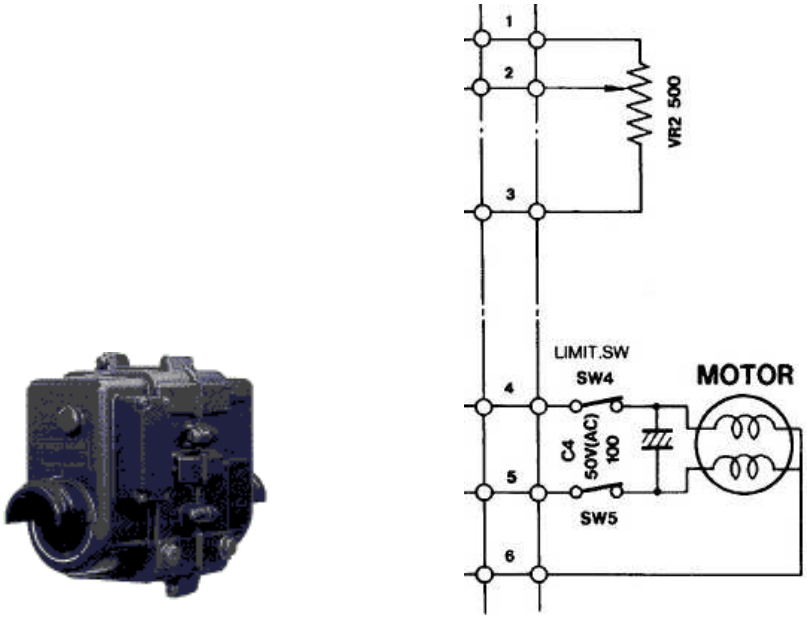

Figure A.3: Antenna rotator picture and electrical schematic. An automatic antenna rotation feature was added to this radar system. The incidence angle can be automatically set from the ground without the need to lower the tower. The voltage between pins 1 and 2 is proportional to the angular position of the rotator

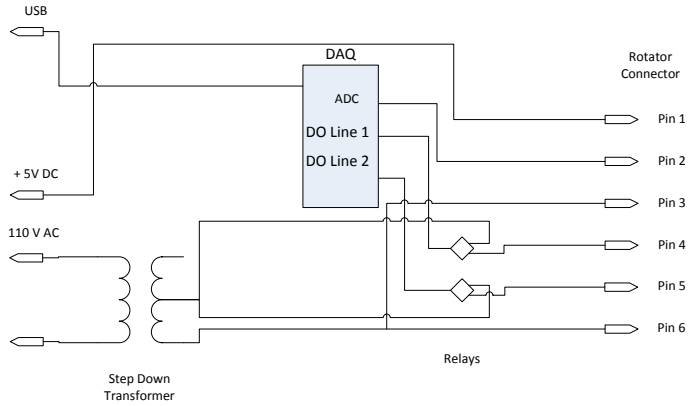

Figure A.4: A simplified rotator controller schematic. This custom controller allows for remote control of the rotator.

power levels with solid state switches. The video leakage is mostly a lower frequency signal which and can be filtered out using bandpass or high pass filters.

BIBLIOGRAPHY

BIBLIOGRAPHY

[1] S. O. Rice. Reflection of electromagnetic waves from slightly rough surfaces. *Commun. Pure Appl. Math*, 4:351–378, 1951.

[2] J. T. Johnson. Third-order small perturbation method for scattering from dielectric rough surfaces. *J. Opt. Soc. Amer. A, Opt. Image Sci.*, 16:2720–2736, 1999.

[3] A. Tabatabaeenejad and M. Moghaddam. Bistatic scattering from three-dimensional layered rough surfaces. *IEEE Trans. on Geoscience and Remote Sensing*, 48, 2006.

[4] Brown G. S R. T. Marchand R. T. On the use of finite surfaces in the numerical prediction of rough surface scattering. *IEEE Transactions on Antennas and Propagation*, 47:600–604, 1999.

[5] Ao C. O. Shih S. E. Yang Y. E. Ding K. H. Kong J. A. Tsang L. Braunisch H., Zhang Y. Tapered wave with dominant polarization state for all angles of incidence. *IEEE Transactions on Antennas and Propagation*, 48:1086–1096, 2000.

[6] C. H. Kuo and M. Moghaddam. Electromagnetic scattering from multilayer rough surfaces with arbitrary dielectric profiles for remote sensing of subsurface soil moisture. *IEEE Trans. on Geoscience and Remote Sensing*, 45:349–366, 2007.

[7] P.C. Waterman. Matrix formulation of electromagnetic scattering. *Proc. IEEE*, 53, 1965.

[8] Moghaddam Mahta Chih-Hao Kuo. Electromagnetic scattering from a buried cylinder in layered media with rough interfaces. *IEEE Trans. Antennas Propagat.*, 54, 2006.

[9] Chen C. Kuloglu M. Ground penetrating radar for tunnel detection. *IGARSS Proceedings*, 2010.

[10] Daniels J. Radzevicius S. Ground penetrating radar polarization and scattering from cylinders. *Journal of Applied Geophysics*, 45:111–125, 2000.

[11] Xu C. Zhang Y., Gong Z. Relationship between mom and t-matrix approach: Tm case in 2-d conducting scattering problems. *Proc. ICMMT*, 1998.

[12] William Menke. *Geophysical Data Analysis: Discrete Inverse Theory*. Academic Press, 1989.

[13] E Polak. Computational methods in optimization. *Academic Press*, 2.3, 1971.

[14] C. Martini S. Ridella A. Corana, M. Marchesi. Minimizing multimodal functions of continuous variables with the "simulated annealing" algorithm. *ACM Trans. on Mathematical Software*, 13, 1987.

[15] A. Tabatabaeenejad and M. Moghaddam. Inversion of dielectric properties of layered rough surface using the simulated annealing method. *IEEE Trans. Geosci. Remote Sensing*, 47:2035–2046, 2009.

[16] Dobson M. Ulaby F, Baltlivala P. Microwave backscatter dependence on surface roughness, soil moisture, and soil texture: Part i - bare soil. *IEEE Trans. Geosci. Remote Sensing*, 16, 1978.

[17] Daniels D. *Ground Penetrating Radar*. The Institution of Engineering and Technology, 2004.

[18] Y. Rahmat-Samii E. Rodriguez D. Entekhabi D. Moller J. Hoffman L. Pierce Moghaddam, M. Microwave observatory of subcanopy and subsurface (moss): A mission concept for global deep and subcanopy soil moisture observations. *IEEE Trans. Geosci. Remote Sensing*, 45:2630–2644, 2007.

[19] Y. Goykhman and M. Moghaddam. An efficient forward scattering model for a three layer medium representing bodies of fresh water. In *Proc. IEEE-URSI*, 2008.

[20] S. L. Chuang and J. A. Kong. Scattering of waves from periodic surfaces. *Proceedings of the IEEE*, 69:1132–1144, 1981.

[21] K.-H. Ding L. Tsang, J. A. Kong and C. O. Ao. *Scattering of Electromagnetic Waves - Numerical Simulations*. New York: Wiley, 2001.

[22] Madrazo A. and Maradudin A. Numerical solutions of the reduced rayleigh equation for the scattering of electromagnetic waves from rough dielectric films on perfectly conducting substrates. *Optics Communications*, 134:251–263, 1997.

[23] J. A. Kong L. Tsang and R. T. Shin. *Theory of Microwave Remote Sensing*. Wiley, 1985.

[24] Mittra R Peterson A., Ray S. *Computational Methods for Electromagnetics*. IEEE Press, 1997.

[25] C. Balanis. *Advanced Engineering Electromagnetics*. Whiley, 1989.

[26] H. Toyama K. Yasumoto and R. Kushta. Accurate analysis of two-dimensional electromagnetic scattering from multilayered periodic arrays of circular cylinders using lattice sums technique. *IEEE Trans. Antennas Propagat.*, 52:2603–2611, 2004.

[27] H. Toyama and K. Yasumoto. Electromagnetic scattering from periodic arrays of composite circular cylinder with internal cylindrical scatterers. *Progress in Electromagnetics Research*, 52:321–333, 2005.

[28] M. Moghaddam and S. Saatchi. Monitoring tree moisture using an estimation algorithm applied to sar data from boreas. *IEEE Trans. Geosci. Remote Sensing*, 37:901–916, 1999.

[29] Y. Goykhman and M. Moghaddam. Retrieval of subsurface parameters for three-layer media. In *IEEE-IGARSS09*, 2009.

[30] Dobson M. Peplinski N., Ulaby F. Dielectric properties of soils in the .3-1.3 ghz range. *IEEE Transactions on Geoscience and Remote Sensing*, 33, 1995.

[31] Duan X. and Moghaddam M. Stabilized extended boundary condition method for 3d electromagnetic scattering from arbitrary random rough surfaces. *APSURSI*, 2010.

[32] K. Elsherbini, A. Sarabandi. Compact high-isolation directive uwb transmit/receive antenna pair for radar applications. *APSURSI*, 2009.